Nonlinear Electronic Transport and Structure Formation in Semiconductors

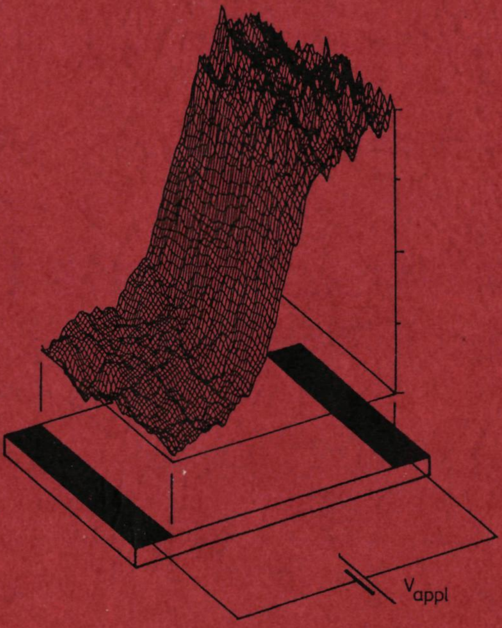

Bert Willing

Nonlinear Electronic Transport and Structure Formation in Semiconductors

een wetenschappelijke proeve op het gebied van
de Natuurwetenschappen

Proefschrift

ter verkrijging van de graad van doctor aan
de Katholieke Universiteit Nijmegen
volgens besluit van het College van Decanen
in het openbaar te verdedigen op
dinsdag 25 oktober 1994
des namiddags om 1:30 uur precies

door

Bert Willing

geboren op 6 juni 1964
te Neuburg (Duitsland)

Druk: Dissertations-Druck, Darmstadt (Duitsland)

Promotores: Prof.dr.ir. J.C.Maan
Prof.dr. P.Wyder

ISBN 90 - 9007641 - 7

Prof. Peter Wyder I owe the opportunity to prepare this thesis at the Grenoble High Magnetic Field Laboratory - although the name of this lab is the only context in which the word "magnetic field" appears in this work.

I'd like to thank Jan-Kees Maan, meanwhile also both professor and boss of a high magnetic field lab, for his acceptance of a German PhD student he never had the possibility to interview before hiring. I am also grateful to him for not asking me every Monday morning about the progress of the work but letting me follow my own projects - and a good idea of his.

Kees de Kort from the Philips NatLab in Eindhoven helped me a great deal on the step from nicely colored pictures to calibrated experimental data. Without his technical hints, the physical content of this thesis would have been much harder to achieve.

Joachim Peinke I thank for the discussions which taught me a lot about nonlinear systems. I am somewhat sorry that this work turned out to cling rather to semiconductor physics than to deterministic chaos. But I also appreciate some "private" evenings with him - and I thank him for his reliable replacement of my old Citroën.

With Jerzey Lusakowski and Prof.Grynberg from the Varszov University I am glad to have had some interesting discussions about those slow domains in GaAs.

Of course I also say thanks to Hans Dresler and his staff from the mechanical workshop for the components they supplied me with, as well as to André Plante and his staff from the "atelier électronique". Herberth Krath I owe many thanks for his help on my optical beamline and for some hints on good French wine.

I shouldn't forget to thank Hartmut Buhmann, now living on a moist island bordering Europe, for tempting me to come to France. I had a most pleasant time together with him, Sabine, Peter, Gudrun, Jan-Jaap, Daniel, Antoine, Birgit and many other students of the CNRS labs.

I owe special to Jan-Jaap who was so kind to act as a translator for the Dutch conclusion of this thesis and to Tina, who helped a lot on my written English. And last but not least, I certainly don't forget here Brigitte, with whom the discussions about Life, the Universe and Everything hopefully won't stop.

"We dance round in a ring and suppose,
But the Secret sits in the middle and knows."

Robert Frost

Contents

1

Introduction

The study of electronic transport is the most basic one in Solid State Physics. Usually such studies are performed at low electric fields where the conductivity is strictly linear and Ohm's law $j = \sigma E$ holds. Most metallic conductors are described very well by this linear law and detailed information such as mean free path or scattering times can be inferred from conductivity measurements as a function of temperature, magnetic field, impurity content etc. The corresponding models are based on spatial homogeneity and invoke equilibrium mechanisms for transport throughout the macroscopic sample.

In this thesis we will deal with strongly nonlinear conductivity ($j = \sigma(E)E$) in a material of very high resistance, namely semi-insulating GaAs. Mechanisms for nonlinearities are numerous but can be reduced in this case to two basic processes: One is the carrier multiplication via avalanches of secondary electrons which are ionized by primary electrons having gained sufficient energy in the applied electric field. The second one is the slowing down of fast carriers, either because their energy is only sufficient to excite impurities but not to ionize them, or because their mobility decreases at high fields due to band structure effects. Either case leads to a spontaneous structure formation within the sample. Avalanches correspond to a filamentary structure, i.e. highly conducting paths in parallel to low conducting ones whereas the second case produces high electric field domains in series with low field areas.

This structure formation indicates a dramatic change in the physics of the system since it is obviously no longer possible to attribute a "bulk conduction" to the sample. Moreover, the structures are often not stable and drift through the sample, eventually resulting in periodic variations of the externally observed voltage or current which make it difficult to assume equilibrium mechanisms. A study of these phenomena has therefore to involve an experimental setup which is able to measure the potential in the sample as a function of position and time. In this thesis we describe such a setup developed by us and discuss the thereby obtained experimental results.

The story of nonlinear transport in GaAs begun in 1961, when Watkins and Ridley [1] predicted a negative differential conductivity (NDC) which should lead to the formation of high-field domains in n-type GaAs. This was experimentally confirmed by Gunn [2] in 1963. The mechanism is meanwhile well understood by a model of scattering of conduction electrons into a subband of higher effective mass [3] [4]. So-called Transferred Electron Devices, like Gunn diodes for microwave generation, make use of this Gunn effect and are of big commercial interest.

About the same time, Barraud [5] and Northrop [6] reported domain formation in semi-insulating (SI-) GaAs. Here, the velocity of the domains was about six orders of magnitude lower than the one of Gunn domains. Additionally, the critical field for onset of domains was reported to be approximately one third of the threshold field for Gunn effect ($E_{c,Gunn} = 3.1 \cdot 10^5\,\mathrm{Vm}^{-1}$). Much experimental work has been done in the following 15 years which led to the development of a theory based on field-enhanced trapping of electrons in a deep level (Sacks and Milnes [7], Ridley and Wisbey [8]). This theory has been commonly accepted, although it was never tested in experimental detail.

The subject saw its revival in the middle of the eighties within the context of deterministic chaos which was found to be a new approach to describe a nonlinear system. Several groups (Maracas et al. [9], Lusakowski et al. [10] [11], Požela et al. [12] , Schöll [13] [14]) were able to show that the nonlinear characteristic of a SI-GaAs sample can be used to drive it onto a route to chaos. Apart from these efforts to embed the slow domains into the more general field of chaotic systems, the development of GaAs-technology for integrated circuits requested a better understanding of nonlinearities in the semi-insulating wafer material. Nowadays, the reduction of the separation between adjacent devices implies electric fields in the order of some 10^6 V/m which are imposed to the semi-insulating GaAs (although the voltages of only few volts within integrated circuits are rather low) [15]. It is evident that circuit manufacturers want to control any kinds of nonlinearities in order not to produce "statistically" operating devices.

Both theory and experiment were handicapped by the fact that theory was made for infinite samples - which rarely exist. Experiments were instead performed on finite samples with metallic contacts whose properties are almost impossible to integrate into theory. Apart from purely qualitative picturing methods (Maracas [16] [15], Rajbenbach et al. [17], Rau [18]), experiments so far have been restricted to measure the total current, partly in connection with a spatially resolved light irridation technique [19]. But as the total current integrates over contacts and bulk sample, it is very difficult to interpret the results on contributions of either part. In other words, theory does not describe a real sample and experiment can hardly decide on the contribution of the bulk. Nevertheless, we present a review of the theory of domain formation in the following chapter.

In this work, we approach the problem by an electrooptic setup, which we derived from the spot-like voltage probing technique originally developed by Fontein et al. [20] [21]. It enables us to look "right into the sample" and to measure its two-dimensional voltage distribution with high spatial and temporal resolution (Fig. 1.1). It is evident that such an experiment can provide us with much more detailed data about the sample than it had been possible up to date. An additional advantage of this setup is that it prevents the probing light to interact with the nonlinear sample. The principles of operation of this setup and its technical design are discussed in the third chapter (and in the appendix).

The fourth chapter discussing the experimental results is divided into three sections. The first one introduces to the phenomenology of domains by connecting qualitative camera frames to the total current at different points of the current-voltage characteristic. This allows us to define the basic regimes of operation: stable sample (no oscillations at all), small oscillations (restricted domains) and pulse-like oscillations (huge domains). Further on, we investigate the topological aspects of domain propagation. It is shown that the topology of domains is directly connected to the shape of the contacts. A simple change in the contacts' geometry results in strong changes to the domain propagation which points to interesting future experiments.

Using quantitative measurements $V(x, y, t)$, the second section concentrates on critical fields for the onset of oscillation and on the overall electric behaviour of the sample during a stable domain cycle. We see that the different kinds of oscillation observed as a function of the applied voltage are due

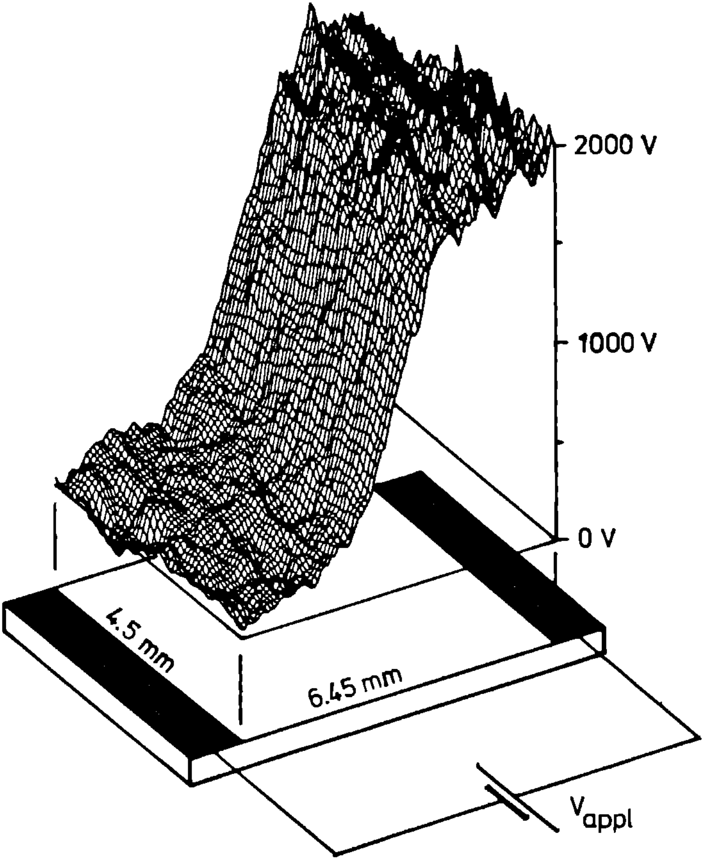

Figure 1.1 :

Typical result of the voltage distribution in a sample (bottom, with parallel contacts) measured with our setup. Here, almost all voltage drops in the middle of the bulk sample; this region represents an high-field domain and drifts with ≈ 0.06 m/s *from the left (cathode) to the right (anode). The density of this surface grid is reduced by a factor of 25 compared to the data delivered by the setup. The exposure time of the camera is* 50 μs.

to the oscillation of different subsystems of the sample, namely bulk GaAs and contact regions, respectively The current during a domain cycle can be clearly split up into the separate contributions from these oscillatory systems Finally, we demonstrate their nonlinear interaction and propose a mechanism which can qualitatively explain chaotic features

The last section deals with the propagation of stable domains in the bulk sample As we can neglect the contribution of the contacts here, we have a direct access to the properties of bulk GaAs The detailed analysis of the structural growth of domains allows us to reconstruct the underlying $j(E)$ characteristic experimentally which, due to the lack of spatially resolved measurements, had not been possible up to now On the basis of this result, we successively discuss the underlying nonlinear parameters (conductivity $\sigma(E)$, free carrier concentration $n_{free}(E)$, space charge $\rho(E)$) Finally, we can conclude on the main features of the capture coefficient $c_{EL2}(E)$ of the involved deep trap which are responsible for the observed fundamental discrepancies between the existing models for slow domains and our experimental facts

2

Domain Formation

In this chapter we will give a brief review of the phenomenology of nonlinear transport and in particular of domain formation We further briefly review the present theoretical and experimental understanding of slow domains in GaAs, showing that the theoretical understanding of this phenomenon is rather scarce Even the most extensive theory by Sacks and Milnes [7], which are almost the only ones to have attempted to model the actual experimental situation, can explain experimental data only by including a wide range of adjustable parameters Although much of our experimental results are in contradiction to this theory, it is helpful to present it, because it contains all the necessary ingredients to arrive at an explanation and gives a basic insight of the phenomenon We will see that much of the lack of understanding stems from the very limited experimental information As we will show later, our experiments allow a much more detailed understanding of the processes determining the structure formation and our results can serve as a basis for a future theoretical approach

2.1 Introduction

Electronic transport is usually described by Ohm's law in which the current density j is taken to be proportional to the electric field E,

$$j = \sigma E = en\mu E \tag{2 1}$$

where σ is the conductivity, n the density of free charge carriers and μ their mobility The mobility incorporates the effect of the scattering of the carriers by imperfections. As long as both μ and n are independent of the electric field, the linear Ohm's law holds. Nonlinearities will occur if either μ and/or n become field dependent. We will briefly discuss the two main cases.

In a sufficiently high electric field, free electrons in a gas may gain enough kinetic energy between two collisions to produce secondary electrons by ionization of atoms, leading to an increase of n as a function of the field (a). On the other hand, just below the critical field for ionization the electrons loose their kinetic energy by ineleastic collisions with atoms. In this case the mobility of the electrons decreases with increasing field while n remains constant (b).

The effect of such mechanisms on the $j(E)$-characteristic of the system is sketched in Figure 2.1. Both characteristics exhibit nonlinearities which are marked by regions of negative differential conductivity (NDC; $\frac{\partial j}{\partial E} < 0$). The avalanche triggered by the high energy electrons of (a) gives a S-shaped $j(E)$-curve and indicates a transition from a low conductive to a high conductive state (electrical breakdown) under increase of the electric field. The decrease of

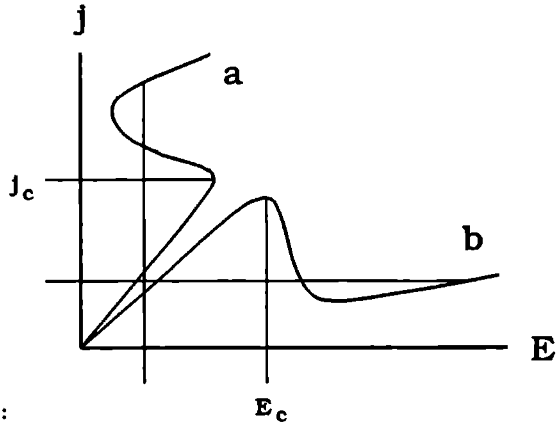

Figure 2.1:

The two fundamental nonlinearities in a j(E)- characteristic: S-shaped (a) and N-shaped (b) negative differential conductivity. Each curve leads to a very characteristic behaviour of the sample mobility in (b) leads to the opposite behaviour, namely a transition from a high conductive to the low conductive state. This is pictured by the according N-shaped $j(E)$-curve. In general, the distinction of N- or S-shaped $j(E)$-curves is a first classification of the different types of nonlinearities. There are numerous mechanisms which produce this behaviour; the two mentioned previously are to be taken as simple examples.

The common feature of these two nonlinear effects is that the system driven into the unstable region reacts by a spontaneous creation of spatial structure. This structure is quite different depending on the shape of $j(E)$. For S-shaped

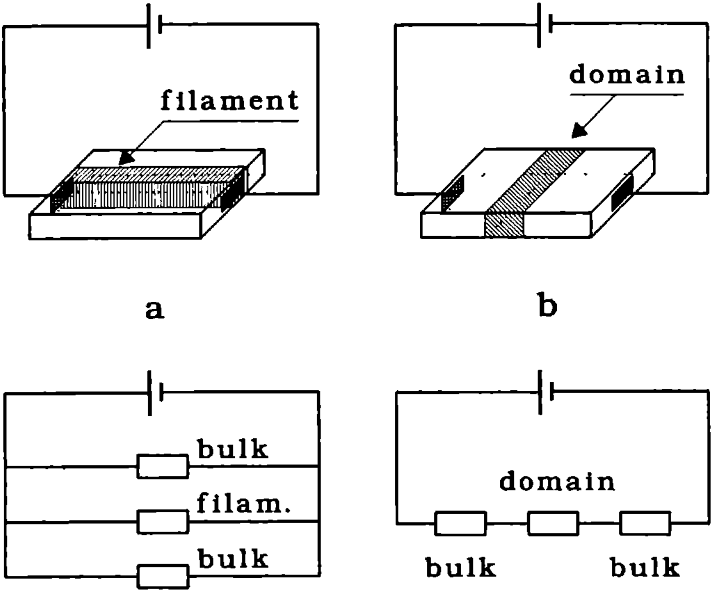

Figure 2.2:

Topological partition of a sample into filaments (a) and domains (b) due to S-$j(E)$ and N-$j(E)$, respectively. (c) and (d) show the according network replacements

$j(E)$, the systems shows three possible values of j for a given E. At any value of j between the critical current density j_c and the local minimum j_{min} we have $\frac{\partial j}{\partial E} < 0$ and j is unstable against small pertubations of E. For the other two possible j it is $\frac{\partial j}{\partial E} > 0$ so that these are stable. Any pertubation will drive the sample off the initial unstable point and will split it into filaments of stable high and low conductivity *parallel* to the current direction (Figure 2.2a). Such high conductivity channels can be observed as a laboratory gas discharge or - more spectacular - as lightnings in a thunderstorm. Experimentally, this state is reached by controlled variation of the total current through the sample (current-controlled instability). The physics of these kind of instabilities in different systems is widely discussed elsewhere [22] [23] [14] [12] [24] [25] [26].

Similarly, for a N-shaped $j(E)$-curve there exist three possible values of E for a given j, one of them being unstable. Here, the sample separates itself into regions of stable high and low conductivity *perpendicular* to the current direction (Figure 2.2b). Because it can be regarded as a serial network of high and low resistors, most of the applied voltage drops over the region of low conductivity wherefore the latter represents a so-called high-field domain embedded between low-field regions. Contrary to a S-$j(E)$ sample, the N-$j(E)$ state is experimentally investigated by controlling the applied voltage (voltage-controlled instability).

2.2 Domains

One of the most studied nonlinearities is the one due to the transfer of electrons under strong electric field from the Γ-point in the GaAs conduction band to the L-point. Since the effective mass at the L-point is much higher ($0.35\, m_e$ at L instead of $0.06\, m_e$ at Γ), the mobility drops drastically upon this transfer. It is the origin of the so-called Gunn domains which are nucleated in n-type GaAs at electric fields above $E_{c,gunn} = 3.1 \cdot 10^{-6}\,\mathrm{V/m}$. Their high drift velocity (equal to the drift velocity of free carriers, $v_0 \approx 10^4\,\mathrm{m/s}$) is used to create microwave radiation by commercial Gunn diodes.

The domains studied here occur in semi-insulating (SI-) GaAs and are of a quite different nature, showing three main distinctions in respect to Gunn domains:

1. SI-GaAs has carrier concentrations of about $n_0 \approx 10^{13}\,\mathrm{m}^{-3}$ at room temperature and domain formation is observed for contact spacings of a few millimetres. In the case of Gunn domans a stability analysis [27] shows that domains can only form if the product of carrier concentration n and sample length L exceeds a critical value of $\approx 10^{15}\,\mathrm{m}^{-2}$. Obviously, a stability analysis for the domains in SI-GaAs has to include additional parameters.

2. The drift velocity v_D of domains in SI-GaAs is about a factor $10^5 \,..\, 10^7$ lower than the velocity of Gunn domains ($v_D = v_0$). From this stems the denotation "slow domains".

3. The critical field for onset of domain formation was reported [19] [28] [9] to be around $1 \cdot 10^5\,\mathrm{V/m}$ (applied critical voltage divided by contact spacing) instead of $E_{c,Gunn} = 3.1 \cdot 10^5\,\mathrm{V/m}$.

The origin of these differences is to be found in the big difference of doping. SI material is used as a substrate in device production and isolates the discrete devices electrically. As well known, Czochralski grown GaAs presents a natural shallow donor density of $n_d \approx 10^{21}\,\mathrm{m}^{-3}$ (of nonstoichiometric or Si contamination origin) which has to be compensated in order to attain a free carrier concentration of $n_0 \approx 10^{13}\,\mathrm{m}^{-3}$ which is required for the desired resistivities of $10^5 \,..\, 10^6\,\Omega\mathrm{m}$. The compensation technique has changed in the past from doping with Cr atoms serving as deep acceptors to the creation of arsenic antiside defects during crystal growth by the liquid-encapsulated Czochralski (LEC) method. This defect is commonly known as EL2 and produces a near-midgap trap (0.67 eV below the conduction band) of a density of $n_{EL2} \approx 10^{22}\,\mathrm{m}^{-3}$ [29] [30] [31]. EL2 is able to act both as a donor and an acceptor [32].

Consequently, EL2 influences the free carrier concentration by trapping and releasing free electrons. As these processes are generally field-dependent, they provide a nonlinear mechanism additional to the intrinsic intervalley transfer and act on the dynamics of the system. A physical model was developed by Ridley and co-workers [8] [33] [28] as well as by Sacks and Milnes [7] [19] in the beginning of the seventies in order to explain the slow domains. The model proposes that the EL2 trap is surrounded by a repulsive barrier Δ_{trap} (Figure 2.3) due to a negative charge of the non-occupied trap which explains that EL2 can act as a donor and as a trap. To be trapped, electrons either must have gained the necessary energy Δ_{trap} to overcome the barrier by heating through an electric field or have to tunnel through the barrier. This leads from $\sigma(E) = n\mu(E)$ to $\sigma(E) = n(E)\mu(E)$ and explains domain formation at other values of the critical field than $E_{c,gunn}$. Furthermore, since a part of the domain's space charge may be localized in traps, the drift velocity of the domain will be determined by the characteristic time of generation/recombination over these traps.

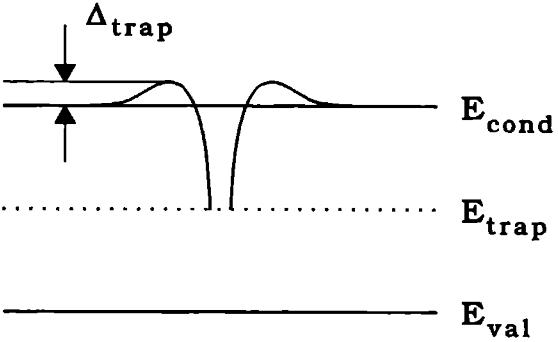

Figure 2.3: *Concept of a trap surrounded by a repulsive barrier*

To describe the electrical behaviour in the presence of traps which capture and emit free carriers, one has to define a rate equation, add ionized traps to Poisson's equation and consider diffusion:

$$\frac{\partial j}{\partial X} + \frac{\partial \rho}{\partial t} = 0 \tag{2.2}$$

$$j = env - e\frac{\partial(Dn)}{\partial X} \tag{2.3}$$

$$\frac{\partial n}{\partial t} = -\frac{1}{e}\frac{\partial j}{\partial X} + gN_t^- - cn(N_t - N_t^-) \tag{2.4}$$

$$\frac{\epsilon}{e}\frac{\partial E}{\partial X} = N_t^- + n - n_0 \tag{2.5}$$

with D the diffusion coefficient, g and c the generation and capture coefficients. N_t, N_t^- denote the total and occupied trap densities, respectively. To this set of equations add the boundary conditions

$$j_0 = en_0v_0 \tag{2.6}$$

for $X \to \pm\infty$ (i.e. far from the domain) and

$$\int_{-\infty}^{\infty} = V_{appl} \tag{2.7}$$

Of the parameters of this system, $v(E)$, $c(E)$ and $n(E)$ are taken as field-dependent ones. On the other hand, diffusion and generation rate are assumed to be independent of the field (the latter is shown to be valid by Makram-Ebeid and Lanno [34] for $E \leq 250 \cdot 10^5\,\mathrm{V/m}$).

The equations 2.2 to 2.5 can be used to investigate the conditions for an initial pertubation ($E_0+\delta E$) to develop into a domain. The analysis (neglecting diffusion) shows that for a pertubation drifting with v_D this will happen if

$$L \cdot [v_0 \frac{(\frac{dN_t^-}{dE}|_{E_0})}{(\frac{dv}{dE}|_{E_0})} + N_{t0}^- - n_0] > \frac{\epsilon v_D}{e(\frac{dv}{dE}|_{E_0})} \tag{2.8}$$

where N_{t0}^- is the density of occupied traps at E_0. For $N_t \to 0$ and $v_D \to v_0$, eq. 2.8 approaches the condition of the Gunn effect $n_0L > \epsilon v_0[e\frac{dv}{dE}|_{E_0}]^{-1}$ [27]. The low drift velocity of domains reduces the right-hand side of eq. 2.8 by a factor of 10^7 in respect to Gunn domains. Additionally, the contribution of the traps to the left-hand side of eq. 2.8 rules out any prediction of its precise value without detailed knowledge of $N_t^-(E)$. We therefore conclude that in contrary to Gunn domains we cannot argue by a simple nL-product about the existence of slow domains.

The time dependence of the initial equations can be eliminated by the transformation into a coordinate system moving with the domain velocity $x = X - v_Dt$ which yields

$$\frac{\partial j}{\partial x} - v_D\frac{\partial \rho}{\partial x} = 0 \tag{2.9}$$

$$j = env - eD\frac{\partial (n)}{\partial x} \tag{2.10}$$

$$v_D\frac{\partial n}{\partial x} = \frac{1}{e}\frac{\partial j}{\partial x} - gN_t^- + cn(N_t - N_t^-) \tag{2.11}$$

$$\frac{\epsilon}{e}\frac{\partial E}{\partial x} = N_t^- + n - n_0 \tag{2.12}$$

As any system of nonlinear partial differential equations, the above system has to be solved numerically. However, this requests a number of parameters which are unfortunately scarcely known. In particular, it is necessary to know the field dependence of the carrier velocity $v(E)$ and of the EL2 capture rate $c(E)$. Under reasonable assumptions of these parameters Sacks and Milnes have calculated a $j(E)$-characteristic which is represented in Figure 2.4 for a carrier concentration of $n_0 = 8 \cdot 10^{14}\,\mathrm{m}^{-3}$ and $N_t = 10^{23}\,\mathrm{m}^{-3}$. The critical field for NDC is calculated to be $E_c = 0.86 \cdot 10^5\,\mathrm{V/m}$ and corresponds well to the range of V_{crit}/L experimentally observed. The characteristic leaves the NDC and becomes stable again at $E_{max} = 32 \cdot 10^5\,\mathrm{V/m}$ which is a strong, qualitative difference to the Gunn effect of which $j(E)$ remains in the NDC region even for very high fields. It has also been possible [7] to model quite reasonably the shape of the domains. As for the drift velocity v_D of the domains, it was found

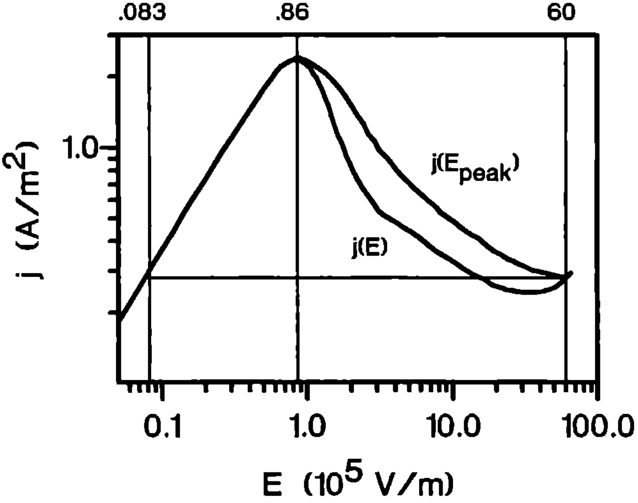

Figure 2.4 : *$j(E)$- and $j(E_{peak})$-characteristic after Sacks and Milnes, 1970*

empirically by Sacks and Milnes [19] as well as by Ridley and co-workers [8] [28] that it should depend on the ratio between free carriers and involved traps as

$$v_D = \frac{n_0}{N_t^-} \cdot v_0 \tag{2.13}$$

This formula gives the right order of magnitude for v_D, because the ratio between carriers and traps (at room temperature and without illumination) is about 10^{-9} and it may be expected that only a small percentage of the traps are occupied. Eq. 2.13 implies that v_D increases linearly with n_0 which was confirmed experimentally by Sacks and Milnes [19], Johnson et al. [31], Knap et al.[11] and Rajbenbach et al. [17]. On the other hand, v_D was shown to either increase or decrease with increasing V_{appl} depending on the order of magnitude of n_0, thus reflecting the influence of the amount of involved traps. Experimental data is inconclusive in this respect. However, eq 2.13 is an empirical finding which is not justified by a deep understanding of the trap behaviour under field.

3

Experimental Aspects

The experimental setup measures the two-dimensional voltage distribution of a sample with high temporal resolution. This is done by use of the electrooptic effect which connects the potential distribution of the sample to a phase shift of detecting light via an electrooptic active crystal. A short, collimated laser beam illuminates this crystal and is reflected through a crossed analyzer into a CCD camera. For any given time, the local voltages can be extracted from the displayed intensity distributions.

In the experiment, the sample is driven into the nonlinear regime by a sufficiently high applied voltage. Domain formation is monitored electrically by temporal variations of the total current. At the same time, these oscillations serve as a trigger for the optical detection of the domains which provides the corresponding voltage distribution of the sample. In the following, we describe the different components of this experiment in more detail.

3.1 Electrical Setup

The main part of the electrical setup consists of a low noise, stabilized power supply[1] which provides the sample with the dc voltage (Figure 3.1). To measure the voltage V_{appl} applied to the sample, the output voltage is divided in parallel to the sample by a voltage divider 1000:1 of a total resistance of $R_{Div} = 10^9\,\Omega$ and read by a multimeter.

---

[1] SODILEC: 0 .. 5000 V or KEPCO BOP 1000M: ± 1000 V

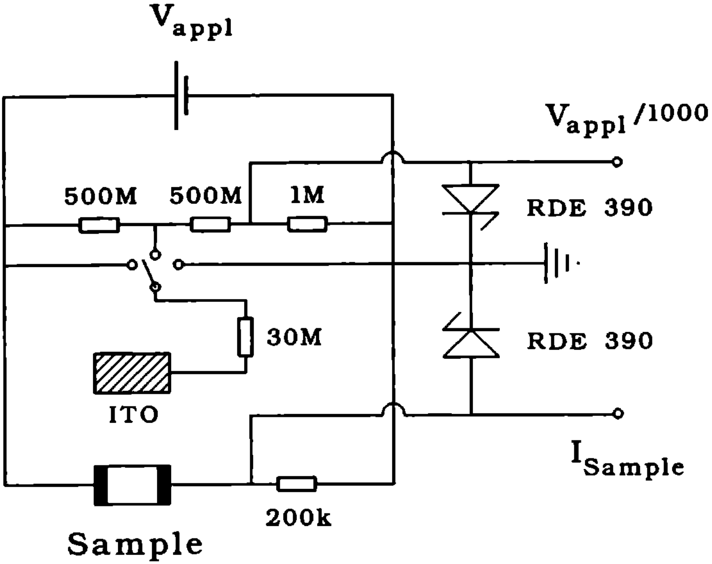

Figure 3.1 : *Electrical Setup*

The total current I_{sample} of the sample is monitored by the voltage drop across a load resistor R_l in series with the sample. In the nonlinear regime the sample develops spontaneous current oscillations which correspond to drastic changes of the sample's resistance. R_l therefore has to be suitably chosen in order not to interfere with the voltage drop over the sample and to provide a sufficiently steep load line. Since relatively high voltages are involved, both monitor outputs are protected by Zener diodes which shunt all voltages above the instrumentation's input limit.

The current signal is fed into an operational amplifier in order to handle the high impedance of the load resistor. The output of this amplifier is then monitored by an oscilloscope, a $x-y$-recorder or a real time Fast Fourier

Analyser[2]. By carefully shielding all leads, we reach a signal-to-noise ratio of ca. -85 dBV.

As we want to investigate the voltage distributions at defined times of the current oscillations, we have to synchronize the optical setup with these oscillations. To this purpose the current signal is used to trigger the CCD camera via a Schmitt trigger.

3.2 Pockels-Effect

Our optical setup is based on the Pockels-effect (electric field induced birefringence) which converts an electric field into a phase shift of light. The birefringence causes a beam of light to experience different velocities on mutually perpendicular axes. For a given polarization of the incident light, its decomposition into the components of different speed and the superposition of those components behind the crystal result in the phase shift of the outcoming light. In the general case, the phase shift Γ is given by

$$\Gamma = \frac{2\pi d}{\lambda}(\Delta n^+ - \Delta n^-) \tag{3.1}$$

where d is the thickness of the crystal and λ the wavelength of the light. The effective changes $\Delta n^\pm$ of the indices of refraction n_0 for light traveling parallel to the unit vector $\mathbf{s}$ and polarization along the unit vector $\mathbf{e}$ are both taken in the crystal axis system. They can be calculated for crystals of the cubic system as

$$\begin{aligned} \Delta n^+ &= -\frac{1}{2} n_0^3 \mathbf{e} \cdot \mathbf{\Delta\beta_k} \cdot \mathbf{e} \\ \Delta n^- &= -\frac{1}{2} n_0^3 (\mathbf{e} \times \mathbf{s}) \cdot \mathbf{\Delta\beta_k} \cdot (\mathbf{e} \times \mathbf{s}) \end{aligned} \tag{3.2}$$

where

$$\mathbf{\Delta\beta_k} = \mathbf{r_{kl}} \mathbf{E_l} \tag{3.3}$$

$\mathbf{r_{kl}}$ is the so-called linear electrooptic tensor of the corresponding crystal. We stress here only the most important point, that is the phase shift depending linearly on the electric field. A detailed analysis of the electrooptic effect can be found in Appendix A.

---

[2] AND AD-3525 FFT Analyser

The main application of the Pockels-effect consists in the amplitude modulation of light which is done by a so-called Pockels cell. Its arrangement of the electric field and the propagation vector of light in respect to the crystal axes are pictured in Fig. 3.2. As the propagation vector of light is parallel to

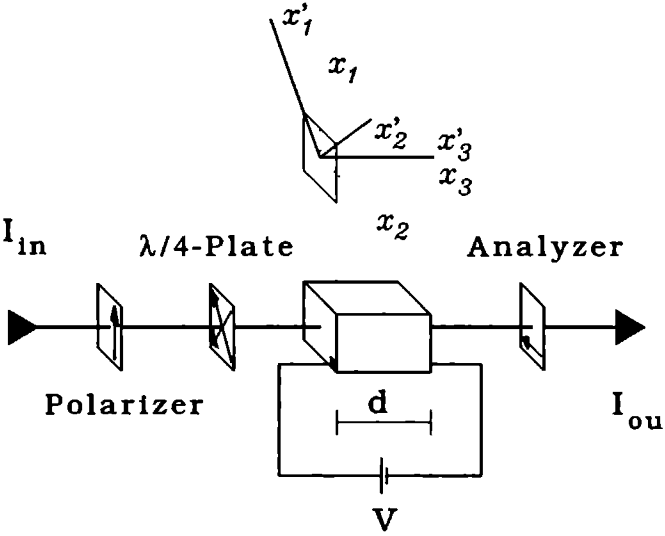

Figure 3.2:

Schematic setup of a Pockels cell. x_i represent the crystal axes whereas x'_i denote the new principal axis system under application of the electric field (for a crystal of the $\bar{4}3m$ group).

the direction of electric field, eq. 3.1 simplifies to

$$\Gamma = \frac{2\pi}{\lambda} n_0^3 r_{41} \; V \qquad (3.4)$$

so that the phase shift is independent of the thickness of the crystal.

To consider the amplitude modulation of light, the amplitude of the incident wave is split up into two orthogonal waves of equal amplitudes $\sqrt{2}E_{opt}$

parallel to x'_1 and x'_2, respectively, which corresponds to an incident intensity of $I_{in} = 4E^2_{opt}$. Due to the retardation Γ, the emerging waves have the amplitudes E_{opt} and $E_{opt} \cdot e^{-i\Gamma}$. By projection of these amplitudes onto x_2 (which is the orientation of our analyzer), the outcoming intensity I_{out} can be calculated as $I_{out} = 4E^2_{opt} \sin^2(\Gamma/2)$ and one obtains

$$\frac{I_{out}}{I_{in}} = \sin^2(\frac{\pi}{\lambda} n_0^3 r_{41} V) \tag{3.5}$$

or, expressing all material constants and the wavelength by the voltage V_π corresponding to a retardation of $\Gamma = \pi$ (that is, $I_{out} = I_{in}$),

$$\frac{I_{out}}{I_{in}} = \sin^2(\frac{\pi}{2} \cdot \frac{V}{V_\pi}) \tag{3.6}$$

where

$$V_\pi = \frac{\lambda}{2n_0^3 r_{41}} \tag{3.7}$$

As it can be seen in eq. 3.5, dI_{out}/dV is very small for low voltages due to the $\sin^2$-term. To overcome this restriction, one uses circular instead of linear polarized light by inserting a quarter-wave plate between linear polarizer and Pockels cell. This adds a fixed retardation of $\Gamma = \pi/2$ to the modulation of the cell, giving

$$\frac{I_{out}}{I_{in}} = \frac{1}{2}[1 + \sin(\pi \cdot \frac{V}{V_\pi})] \tag{3.8}$$

If $(\pi \cdot \frac{V}{V_\pi}) \ll 1$, this equation can be simplified to a linear response function between the applied voltage and the outcoming light intensity for quasi-stationary voltages (Figure 3.3).

If the sample itself is electrooptically active and a reference potential plane can be created, one can directly measure the potential within the sample, as it was performed for the investigation of a two-dimensional electron gas in GaAs/GaAlAs heterostructures [20] [35] [36] [37] [38]. If the sample itself cannot be used for detection, an electrooptically active crystal furnished with a transparent electrode on one side may be placed on top of the sample. A reflective setup measures the difference in potential between this electrode and the surface of the sample [21].

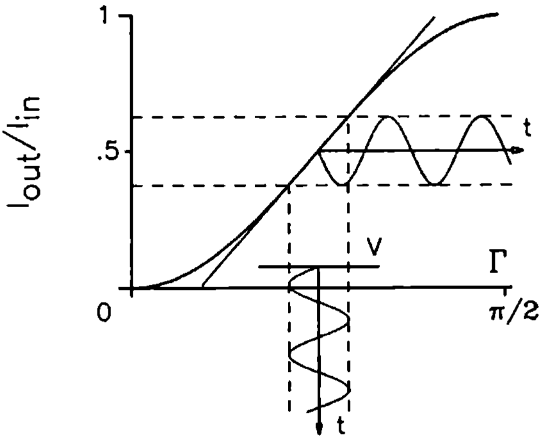

Figure 3.3:
Linear modulation of the amplitude of circular polarized light by a Pockels cell (after Yariv)

3.3 Transmissive Setup

For completeness we also discuss a transmissive setup which we used for qualitative experiments It measures the transmission of the GaAs sample directly between crossed polarizers Since the samples were cut with the < 100 > direction perpendicular to the surface and thus parallel to the propagation vector of the light, no phase shift due to the electrooptic effect was to be expected Nevertheless, we could also observe domains in this configuration Additionally to its electrooptical activity, GaAs shows a strong piezoelectricity which causes mechanical deformations of the crystal lattice due to the high electric field of the domains The contributions of this strain at the surface of the sample induce birefringence via the piezooptic effect (which is analogous to the electrooptic effect) and the resulting phase shift Γ_{surf} is detected by the camera.

To estimate the contribution of Γ_{surf}, we investigated a GaAs sample of $6 \cdot 5 \cdot 0.45\,\mathrm{mm}^3$. Under application of a dc voltage the sample exhibited slow high-field domains with peak electric fields in the order of $E_{peak} \approx 10{\cdot}10^5\,\mathrm{V/m}$. The resulting intensity patterns were compared with a calibration run of the intensity versus homogeneous phase shift. The latter was introduced by an inserted $\lambda/4$-plate and was proportional to the angle between one principal axis of the plate and the polarization vector of the light incident on it.

In fact, the values of Γ_{surf} differ only by a factor of ≈ 1.5 from the electrooptic phase shifts corresponding to the peak fields of domains measured later on (Sec.4.4.2). We can state that, for samples of the usual thickness of commercial GaAs wafers, the surface contribution to the total phase shift distribution is of the same order as the electrooptic contribution and hence our setup is purely qualitative. To achieve a quantitative readout, we have to limit the uncertainty due to surface distortion to about 10 % of the total retardation which means that the thickness of the sample has to be increased by a factor of 10. Furthermore, from the values of the electrooptic and piezooptic coefficients [39] it is not clear whether Γ_{surf} and the electrooptic phase shift have the same algebraic sign so that both contributions may as well add up as they may be concurrent.

Rajbenbach, Verdiell and Huignard [17] invented this transmissive setup in 1988 for the investigation of slow domains in GaAs:Cr. But by using a sample of $d = 3.6\,\mathrm{mm}$ in $< 110 >$ direction, they also were restricted to a qualitative interpretation of their obtained phase shift patterns.

On the other hand, it is clear from this data that, if one is limited to the investigation of thin samples, there is no point to bother about the orientation within a transverse setup as all orientations yield the same information. This makes the setup very versatile for a "fast look" on the domains of a sample if no quantitative recording of electric fields is needed. However, the interaction of the transmissive light with the strongly nonlinear behaviour of the sample in the presence of domains is a serious restriction.

3.4 Reflective Setup

The reflective setup as sketched in Sec 3 2 offers two main advantages Firstly, a precise calibration of the phase shift against applied voltage is possible Secondly, the use of a separate electrooptic crystal instead of the sample itself for detection makes it easy to shield the sample against any penetration of light

The developed setup described in the following consists of three basic units The sample mounted to the electrooptic active crystal, the beamline for conditioning of the probing light and finally, as the detector, a CCD camera connected to a digital image processing system

3.4.1 BSO Crystal

In our setup we use the longitudinal electrooptic effect of the bismuth silicate $Bi_{12}SiO_{20}$ (BSO) This cubic crystal belongs to the symmetry group 23 and shows the same simple electrooptic tensor symmetry as $\bar{4}3$m crystals, i e $r_{41} = r_{52} = r_{63}$ are the only nonvanishing elements BSO is a yellowish, insulating crystal with a band gap of $E_{gap} = 3\ 15\ 3\ 25\,\mathrm{eV}$ ($\equiv \lambda = 394\ 382\,\mathrm{nm}$), a resistivity of $\rho = 5\ \ 10^{11}\,\Omega\mathrm{m}$ and a dielectric constant of $\epsilon = 56$ [40] Its electrooptic activity of $n_0^3 r_{41} = 7\ 8\ \ 10^{-11}\,\mathrm{m/V}$ is about 30 % higher than that of GaAs Figure 3 4 sketches the geometry and orientation of our BSO application The BSO is cut normal to its $< 100 >$ direction, it is this plane which represents the view plane of our setup One of these surfaces is furnished with an anti reflex coating of which the outmost layer is an indium tin oxide (ITO) deposition ITO has a resistivity of typical $\rho = 4\,\Omega\mathrm{m}$ due to impurities and serves as a transparent electrode Placing the BSO with its surface opposite to the ITO electrode onto the surface of the sample and connecting the ITO electrode to a fixed potential in respect to the sample (i e $V_{ITO} = 0$, $V_{ITO} = V_{appl}$ or $V_{ITO} = 0\ 5\ V_{appl}$), we have created a reference potential plane Any voltage distribution $V_{sample}(x_1, x_2)$ is thereby translated into an electric field distribution $E(x_1, x_2)$ along the x_3 direction which we read out by the electrooptic effect According to eq 3 4, a polarized light beam travelling along x_3 undergoes a retardation which is proportional to the integral of $E(x_1, x_2)$ over the BSO thickness d which equals $V_{sample}(x_1, x_2) - V_{ITO}$ To prevent the detecting light beam from entering the sample, the face of the BSO which is in contact with the sample

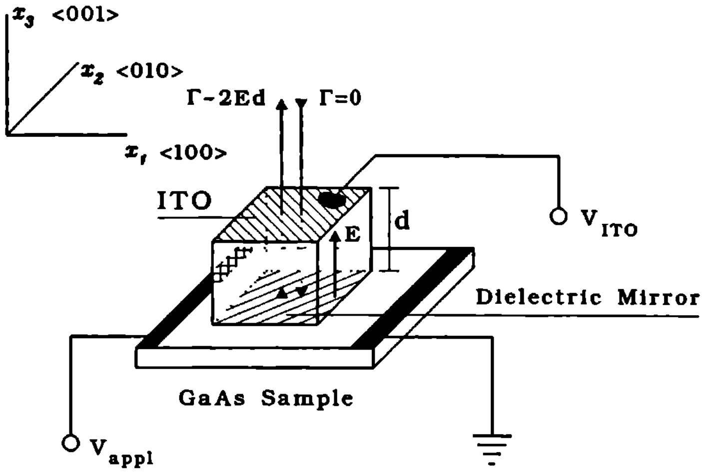

Figure 3.4 : *Orientation and application of the BSO crystal onto the sample*

is covered with a mirror of a transmittance $\leq 10^{-5}$. This mirror is made of dielectric layers in order not to shield the voltage distribution of the sample (and not to shunt it).

This technique was developed by the group of K.de Kort at the Philips NatLab in Eindhoven, The Netherlands, where it has been employed as an optical tool for the quality control of integrated circuits. In their case, no spatial resolution was provided as the laser beam was focussed onto a spot in order to investigate single leads of the circuit. On the other hand, the detection of the phase shift by a photodiode and the use of a lock-in technique allows here a resolution of 10^{-6} radians in the phase shift corresponding to a few millivolts in potential. This resolution is about 3 to 4 orders of magnitude better than the one to be achieved with our two-dimensional technique (Sec. 3.4.4). To test a first spatially resolving setup, K.de Kort kindly lent us two of his BSO crystals with coatings tailored for a wavelength of $\lambda = 780\,\mathrm{nm}$ and having a view field of $1.2 \cdot 1.2\,\mathrm{mm}^2$.

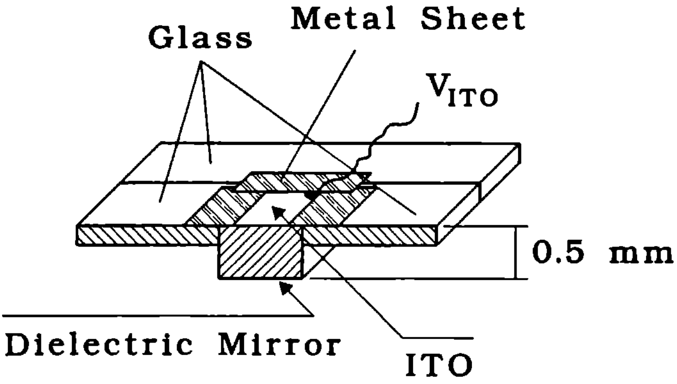

Figure 3.5 : *Mounting of a small BSO crystal in a glass frame*

Because the BSO crystals were much smaller than the samples, it was necessary to move the sample in respect to the BSO (the latter had to remain in its fixed position to the laser beam). The sample was therefore mounted on a $x-y-z$- stage in combination with a table allowing the adjustment of parallelism between sample and BSO. Precaution had to be taken against electric breakdown of the surrounding air ($E_{crit,air} = 11 \cdot 10^5\,\mathrm{V/m}$) because the thickness of the BSO was of $d = 0.5\,\mathrm{mm}$ while the voltage drop between sample and ITO electrode reached $V_{appl} = 2500\,\mathrm{V}$. We therefore introduced a resistor into the lead contacting the ITO electrode which instantly cut down a possible discharge. Figure 3.5 sketches the mounting of the BSO in a frame of 0.15 mm thick glass plates. Black colored metal sheets were used to optically shield the outer parts of the (100)-surfaces which had not been covered by the dielectric mirror.

At a later stage, a new crystal with a size of $10 \cdot 10 \cdot 5\,\mathrm{mm}^3$ and coatings[3] tailored to a wavelength of $\lambda = 780\,\mathrm{nm}$ and covering an area of $10 \cdot 9\,\mathrm{mm}^2$ was used. It was thus possible to image the whole sample within a single frame.

---

[3] applied by Laseroptik GmbH, FRG

The suppression of the $x - y - z$-stage of the sample holder now allowed a more compact mounting of the sample together with the BSO in a closed cell (Figure 3.6). This closed mounting offered the further advantage of a more precise temperature control because convection of air could be widely suppressed. The increase of the BSO thickness by a factor of 10 eliminated the risk of gas discharges in air since stray fields outside the crystal were limited to $E_{max} = 5 \cdot 10^5\,\mathrm{V/m}$.

3.4.2 Beamline and Camera System

We use a semiconductor laser diode[4] with a wavelength of $\lambda = 780\,\mathrm{nm}$ and a continuous output of $P_{out} \leq 10 \cdot 10^{-3}\,\mathrm{W}$ mounted in a modular system[5]. The system includes a diode mounting module which serves as a heat sink through its heat capacity and a collimating triple lens module. By factory adjustment, the emerging beam has a cross section of $1.5 \cdot 4.9\,\mathrm{mm}^2$ with a cone angle of $6 \cdot 10^{-2}$ degree. The beam is brought into square shape by means of two cylindrical lenses (Figue 3.7). According to the view field of the respective BSO crystal in use, the beam is widened symmetrically in a second step before passing a Glann-Thompson polarizer. After reflection at the dielectric mirror, the beam is coupled by a 50 % beam splitter through a crossed analyzer (also Glann-Thompson) into the aperture of the CCD camera. The beam splitter was chosen to be a double glass prism because a metallic 50 % filter (the cheaper solution) would introduce a parasitic phase shift due to its metal coating.

The principal difficulty of this setup is the coherence of laser radiation which gives rise to various speckle patterns in the CCD frames and thereby complicates the numerical processing of the frames. The use of monochromatic light is necessary since the phase retardation depends on the wave length. By coherent light, we introduce interference patterns in the field of vision as well as random speckles. Interference patterns are mostly stripe patterns caused by slight deviations from parallelism of opposite faces of a beam-line component. Random speckles are caused by a inhomogenous intensity distribution of light over the aperture of the laser diode and by dust particles.

We therefore added a second laser diode similar to the first one and merged the two beams by another beam splitter so that the intensity distribution is

---

[4] LT027

[5] SK9650.T5, Schafter & Kirchhoff, FRG

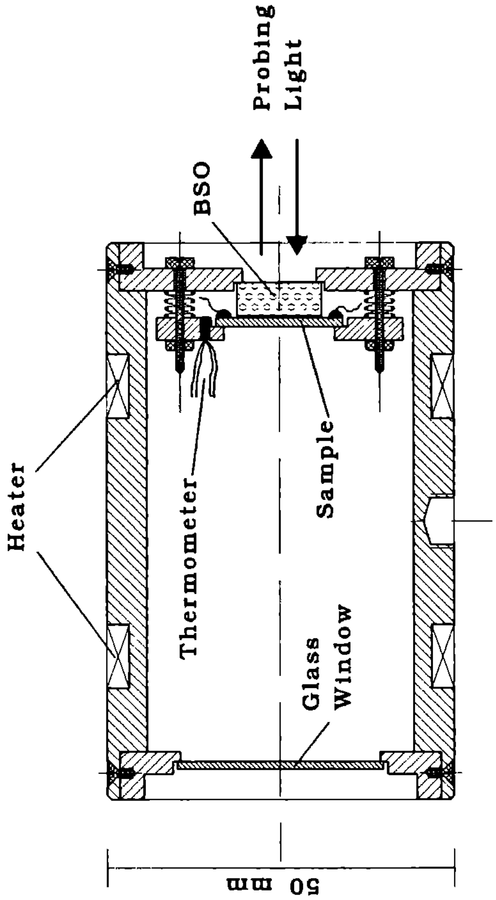

Figure 3.6 : *Mounting of BSO crystal and sample in a closed cell*

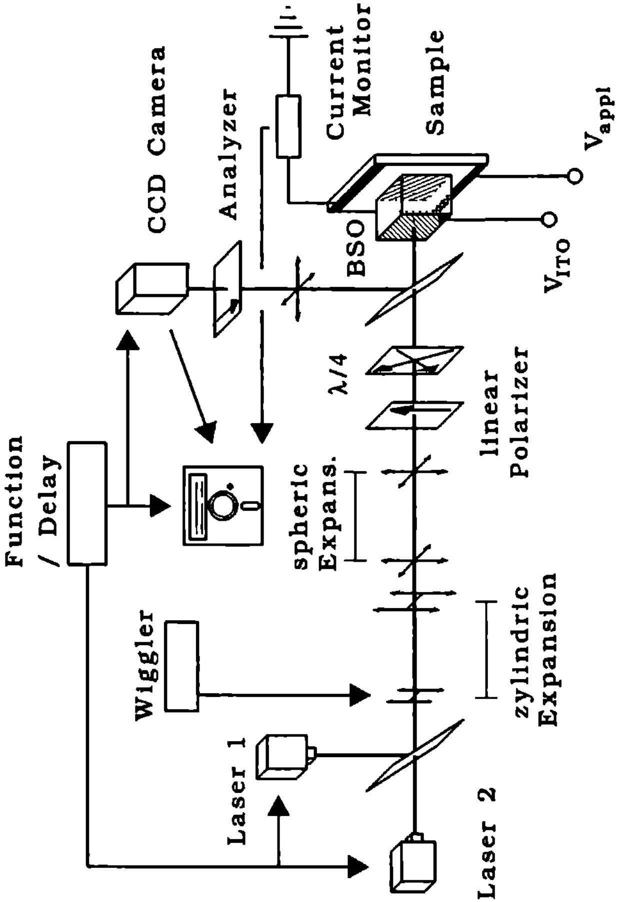

Figure 3.7 : *Scheme of the beam-line for reflective measurements*

smoothed due to the overlay of two independent patterns. Additionally, in the case of stationary measurements in video mode, one of the cylindrical lenses was mounted on a loudspeaker. Driving this loudspeaker with a frequency generator in the audio range, the beam (and with it its speckle pattern) oscillates over the BSO crystal. The mean intensity detected by the camera still shows the patterns in the lateral direction whereas the patterns in the vertical direction are smoothed out quite efficiently. If the camera is triggered to operate sychronized to the current oscillations, the beat between the lens frequency and the current oscillation makes this smoothing technique impossible. Instead, we trigger the laser to give two or three independent pulses (with independent speckle patterns) during each exposure of a frame. Averaging over 256 frames gives a satisfying smooth intensity profile.

The CCD camera[6] is an intensifying CCD video camera. It contains a multichannel plate (MCP, about 15 million channels of a diameter of $12 \cdot 10^{-6}$ m each) with a photocathode on its front side and a phosphor screen on its back side. By changing the acceleration voltage across the MCP, the intensification can be continuously varied between 0 .. 10^4. Apart from the continuous video mode, this voltage also serves as an electric shutter which is closed by reversed voltage and opened for exposure during the acceleration pulse. These pulses can be gated internally within a range of 10^{-8} .. 10^{-3} s or externally to obtain any exposure time up to infinity. Triggering of these pulses is done either internally in video mode or externally for an operation asynchronous to the video norm. The external trigger is fed via a delay line to the camera which allows a continuous sweep of the exposure window over the current cycle of the sample.

The image intensifier with a S25 photocathode has a spectral range of $\lambda = 350$ .. 950 nm with a maximum sensitivity at $\lambda = 580$ nm. The absolute sensitivity at $\lambda = 780$ nm is 20 mAW^{-2} which is about half of the maximum sensitivity.

The output of the camera consists of a frame of 756·580 pixel, each of the digitized to 8 bit. This frame is put into a frame buffer where it lasts until the next trigger clears it for the following frame. Single shots are possible without the need of a hardware trigger on the processing system because the buffer provides the actual frame as a still image in video mode.

---

[6] DiCAM-2, PCO Computer Optics, FRG

For further processing and storage, the frame is taken over by a frame grabber board[7] implemented in a standard 80386 personal computer (PC). This frame grabber has a 1 Mbyte RAM frame buffer which can be handled as one big buffer (1024·1024·8 bit), two deep buffers (512·512·16 bit) or four small buffers (512·512·8 bit). The processing unit on the board in connection with an extra co-processor allows fast and efficient handling and processing of the frames, like binary and algebraic functions between two frames, geometric operations, average of 256 small 8 bit input frames into a 16 bit buffer, contrast enhancement and filtering, edge and object detection etc.

3.4.3 Calibration and Measurement Procedures

A measurement consists of the registration of a measurement frame and the calibration of this intensity distribution into a voltage distribution. The calibration has to be optimized in order to limit the cycles of time-consuming pixel-to-pixel operations (since there are 262144 pixels in each frame) and to reduce the amount of frames to be stored on disk (one frame corresponding to 0.5 Mbyte).

The setup can be operated with linear or circular polarized light. Due to the different sensitivities which have to be combined with the dynamic range of the camera, each method has a preferred range of voltage to detect.

For linear polarized light, the normalized intensity $I^* = I_{out} \cdot I_{in}^{-1}$ and the sensitivity $\mu_l = dI^*/dV$ are given for small voltages (up to ≈ 300 V) by Sec. 3.2

$$I^* \simeq \frac{\pi^2}{4V_\pi^2}(V_{sample} - V_{BSO})^2 \tag{3.9}$$

$$\mu_l \simeq \frac{\pi^2}{2V_\pi^2}(V_{sample} - V_{BSO}) \tag{3.10}$$

Apart from the square dependence which suppresses the sign of the detected voltage, both I^* and μ_l vanish a detected voltage of $0\,V$. We can use the dark video screen at $V_{sample} = 0$ to outweigh the poor μ_l for low voltages by increasing the intensification α_{CCD} of the camera (up to a factor of 10^4) or the laser output. The intensity range of the recorded frame can therefore always be stretched to match the dynamic range of the camera (0 to 8 bit).

---

[7] Matrox MVP-AT/NP ES

For circular polarized light we have

$$I^* \simeq \frac{1}{2}[1 + \frac{\pi}{V_\pi}(V_{sample} - V_{BSO})] \quad (3.11)$$

$$\mu_c \simeq \frac{\pi}{4V_\pi} \quad (3.12)$$

Hence, a detected voltage of zero corresponds to $I^* = 0.5$ independently of α_{CCD} or laser output. The sign of the detected voltage can be determined if we put $V_{BSO} = 0.5 \cdot V_{appl}$ since eq. 3.12 is linear. The dynamic range of the camera can only be matched if $V_{appl} = V_\pi$ (= 5000 V) because then $I^* = 0$ for $V_{sample} = 0$ V and $I^* = 8$ bit for $V_{sample} = V_{appl}$. Obviously, circular polarized light is restricted to the investigation of rather large voltage differences as they are typical for stable domains.

In terms of calibration, operation with linear or circular polarized light has a main distinction: In a frame obtained with linear polarized light, the intensities correspond to a voltage range from 0 V to V_{appl} independently of V_{appl}. Because camera and laser are always adjusted to $V_{appl} \equiv 8$ bit, a voltage drop of 10 V yields exactly the same frame as a drop of 1000 V and we measure the voltages V_{sample} only relatively to V_{appl}.

On the other hand, circular polarized light shifts the zero detected voltage to the camera's 4 bit level and we always measure absolute phase shifts instead of relative ones. The calibration has therefore to establish a function between absolute phase shifts and absolute voltages since resolution and sensitivity cannot be changed by camera or laser but only by replacing the electrooptic crystal.

For both methods, calibration and measurement procedures are almost identical. Calibration firstly determines the intensity (principally of every pixel) as a function of the local voltage and secondly normalizes the intensity distribution of a frame to the distribution of I_{in} (which is not at all homogeneous). This is done by putting the sample on a uniform potential in respect to the BSO and recording the intensity distribution. This frame is normalized pixel to pixel to a frame taken at an homogeneous potential defined for a calibration run ($V_{sample} - V_{BSO} = V_{max,appl}$ for circular and $V_{sample} - V_{BSO} = 0$ for linear polarized light). Since both frames show the same distribution of I_{in}, the resulting frame is quite homogeneous. Repeating this procedure subsequently for various voltage steps one obtains a set of calibration frames containing the desired information (Fig. 3.8 and 3.9). The calibrations performed for linear

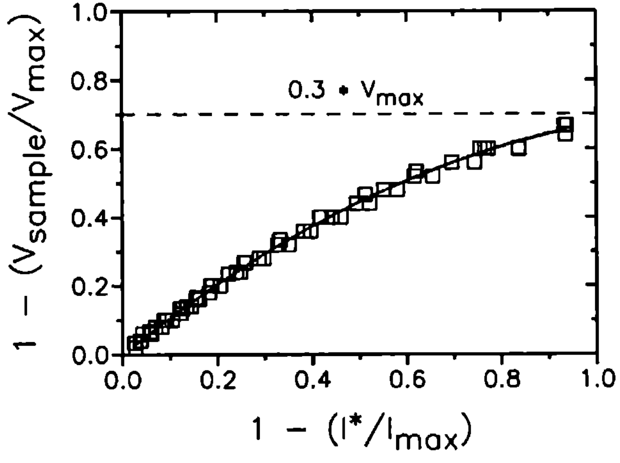

Figure 3.8 : *Calibration for the operation with linear polarized light*

polarized light are neither dependent on the maximum applied voltage nor on the sign of $(V_{sample} - V_{BSO})$. Nevertheless, a calibration has to be done for both methods after every mounting of a sample onto the BSO.

For the measurement procedures, the homogeneous potentials are replaced by the voltage distribution in the sample which may be given by high-field domains etc. Each measurement frame is also normalized to $I_{in}(x, y)$ by the same operation as for the according calibration frames. As already done during calibration, the recording of any frame consists of an average over 256 frames of the same event; the result is put into a 16 bit deep frame. This routine significantly enhances the signal-to-noise ratio and allows a scaling of the intensities better than the 8 bit of the camera.

While for circular polarized light all pixels of a measurement frame can be calibrated, this is not possible for linear polarized light. Here, the poor sensitivity around zero detected voltage in connection with the non-vanishing offset noise of the camera allows only a calibration of the pixels in the range of

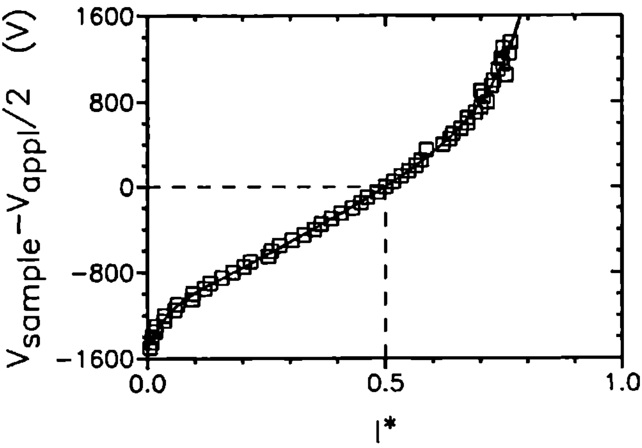

Figure 3.9 : *Calibration for the operation with circular polarized light*

$0.3 \cdot V_{max} .. V_{max}$ (Fig. 3.8). In order to obtain the full information one has to repeat the measurement with this time the BSO put to $V_{BSO} = V_{max}$ so that the second frame contains the pixels of $0 .. 0.7 \cdot V_{max}$.

3.4.4 Performance and Possible Improvements

Voltage resolution for linearly polarized light is a relative one, since we measure voltages relatively to the applied voltage. The calibration runs show that the accuracy is about 1 % of V_{appl} around the 16 bit level of the measurement frame. At the lower parts of the frame, i.e. for levels corresponding to $\approx 0.3 \cdot V_{appl}$, accuracy is not better than 5 % of V_{appl}. This decrease in accuracy is due to the decreasing signal-to-noise ratio for low intensities.

Operation with circulary polarized light yields an absolute voltage resolution of $\Delta(V - 0.5 \cdot V_{appl}) = 10 .. 15$ V for every pixel of the frame.The accuracy is then given by $\Delta(V - 0.5 \cdot V_{appl})/0.5 \cdot V_{appl} = 5 .. 1$ % for $V_{appl} = 200 .. 2500$ V. From a comparison of the two resolutions it is evident that at low V_{appl} ($\leq 200\,\mathrm{V}$) linearly polarized light is to be preferred in spite of the more complicated measurement routine. At higher voltages, corresponding in our case to the regime of stable domains, we can combine the better accuracy and the simple mode of operation of circularly polarized light.

In terms of temporal resolution, the achieved signal-to-noise ratio together with α_{CCD} gives us a minimum exposure window of $\delta t = 50\,\mu\mathrm{s}$. This is by no means a limit for the investigation of slow domains which show drift velocities of $v_D = 0.001\,..\,0.1\,\mathrm{m/s}$. Here, the drift of the domain during the exposure window is $\delta x \approx 5\,\mu\mathrm{m}$ corresponding to about 3 frame pixels. For the case of circularly polarized light, the lower limit for the exposure window was not needed to be reached.

A major limit of an enhanced resolution is the interference pattern within the field of vision in connection with the dynamic range of the camera. This is a general problem for image processing systems, because here we cannot sweep the laser beam off a dust particle on a beam-line device as it can be done in a spot-like measurement. Apart from the averaging routines described in Sec. 3.4, all one can do is to stop smoking in the lab.

Another target for improvements is the adjustment of the laser's wavelength to the maximum spectral sensitivity of the photocathode mounted on the camera. The only restriction to the laser is that the electrooptic crystal has to be transparent for the chosen wavelength. As BSO has a bandgap corresponding to $\lambda = 390\,\mathrm{nm}$, it is no problem to match the laser with the peak of the camera at $\lambda \approx 580\,\mathrm{nm}$. Due to the chronological development of our setup we ended up with $\lambda = 780\,\mathrm{nm}$ which means a decrease in α_{CCD} by a factor of ≈ 20. However, an improvement in spectral sensitivity as well as the possible choice of a more sensitive electrooptic crystal (defined by a lower V_π) is important for an enhanced signal-to-noise ratio only for the detection of low voltage levels using linearly polarized light. At higher voltages, a lowered V_π would rather limit the setup.

An enhanced signal-to-noise ratio is definitively needed if we want to expand the setup to single shots. For the presented measurements, all frames were taken as an average over 256 frames of an identical, periodic event. To achieve the same signal-to-noise ratio for one single shot, one should use a cooled camera head to reduce the noise level. Additionally, the computational software should allow a fourier transformation of the frames which makes it possible to remove intensity fluctuations below a certain length scale.

Apart from the voltage resolution, a serious problem is the correct mounting of the BSO onto the sample since the quality of the frames is most sensitive to a parallel contact between BSO and sample. For the setup working with the small BSO, it was possible to monitor the sample's approach to the BSO on the screen via the induced phase shift distribution. As for the mounting in the closed cell, no satisfying solution was found. Here, the only hint for a homogeneous contact between crystal and sample was found to be the distribution of interference fringes produced by the thin layer of air between the two components. The fringes could be observed in white light; any inhomogenity here could be taken as evidence for a peak of mechanical pressure. However, the positioning could be checked definitely only after closing the cell and adjustment of the beamline, a procedure which soon becomes nerve-racking.

4

Experimental Results

The experiments described in this chapter show that the step from measurements of only current and voltage between contacts, as done in the past, to our time-resolved voltage distributions is quite huge. As even a single frame contains a large amount of detailed data, already a relative small number of experiments already allows us to describe the physics of domains much more precisely than it has ben possible on the basis of several years' integral measurements.

This chapter is organized as follows: in a first section, after a general discussion of the samples, we present the phenomenon of domains in SI-GaAs qualitatively. By connecting time series of frames picturing the domain cycle to the temporal evolution of the current, it becomes evident that in a first approach, the domain can be described by a high resistance which switches the current between low and high levels upon its creation and annihilation. The finding that a change in the topology of the domain leads to a drastic change in its dynamics gives an outlook to interesting experiments to be performed in future.

The second section focuses on this domain cycle. By measuring the local critical fields it is shown that a sample is in fact composed of two nonlinear subsystems, i.e. contact regions and bulk GaAs. Each region has its own range of critical fields and contributes to different regimes of the current-voltage characteristic. The typical spontaneous current oscillations connected to the propagation of a stable domain are shown to result from a nonlinear interaction between the two subsystems. We propose a mechanism leading from this interaction to a route to chaos as it was observed by other workers. On the basis of these result we can now also explain why the ring-shaped domains created by a circular cathode have a maximum radius of propagation.

In the following, we deal with the features of stable domain propagation in the bulk itself where there is no influence of the contacts. The structure of the domains is shown to be based entirely on the properties of bulk GaAs. Due to the spatial resolution of the voltage distributions obtained by our setup, we can gain detailed information about the growth and the shape of the domains as a function of their control parameter. This enables us to reconstruct field-dependent characteristics such as current density, free carrier concentration and amount of the involved space charge. The latter quantity is shown to be equal to the concentration of ionized traps. Finally, we can assemble all information in order to determine the main features of the field dependence of the trap's capture coefficient. The comparison of our data with the predictions made by the models of field-enhanced trapping shows that the latter can be taken only as a starting point, as they already miss the proper stability of the domain structure.

4.1 Samples and Phenomenology

All samples investigated were prepared from LEC grown, unintentionally doped single crystal GaAs-wafers (Sumitomo). The low field mobility μ_0 is given by Sumitomo as $\mu_0 = 0.5\,\mathrm{m}^2/\mathrm{Vs}$. The density of deep levels (i.e EL2: arsenide antiside defect) was not measured, but in this material the EL2 density is about $n_{EL2} = 2 \cdot 10^{22}\,\mathrm{m}^{-3}$ [15].

The samples were cut to different sizes, all with a thickness of $d = 0.45\,\mathrm{mm}$ and the sides in $< 100 >$-direction. Contacts were either parallel stripes with contact spacings of $L = 1..10\,\mathrm{mm}$ or two circular dots with distances of $2..5\,\mathrm{mm}$ and diameters of $\o \approx 1\,\mathrm{mm}$. The materials used as contacts were In (pressed onto the sample), Au, Sn or an eutectic alloy of Au/Ge containing 6 % Ni. The last three materials were evaporated with a thickness of about $0.2\,\mu\mathrm{m}$ and annealed during 10 min at 420 °C under inertial gas atmosphere to provide a diffusive implementation into the bulk GaAs as well as mechanical stability.

Figure 4.1 shows a typical current-voltage $(I(V_{appl}))$- characteristic obtained for most SI-GaAs samples of a contact spacing $L \geq 2\,\mathrm{mm}$ and similar

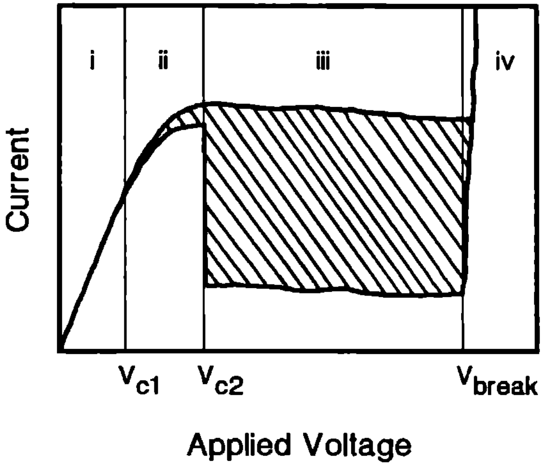

Figure 4.1 :

Typical $I(V_{appl})$-characteristic of a sample, revealing four different regimes: i. linearity, ii. small sinoidal oscillations, iii. large pulse-like oscillations, iv. electrical breakdown. The upper and lower curves represent maximum and minimum current between which the system oscillates (hatched area).

as reported in the literature [31] [10] [41] [18] [42] [32]. Raising V_{appl}, both total current and video screen (monitoring the real- time voltage distribution) distinguish four regimes:

i. Up to a first critical applied voltage V_{c1}, the (slightly sublinear) characteristic is smooth and the video screen shows that the voltage distribution is stable over the whole contact spacing. While the field is homogeneous over most of the sample, the voltage drop in the vicinity of the cathode is distinctly enlarged implying an enhanced field due to a depletion layer at the cathode.

ii. Exceeding V_{c1}, small sinoidal oscillations with frequencies of 1 .. 100 Hz appear on the dc component of the current. Their amplitude grows smoothly with voltage and reaches about 5..15 % of the total current signal. On the screen, the voltage distribution becomes unstable at isolated points of the cathode border. Weak domains propagating as fluctuations of the field from the cathode in the direction of the anode are seen. These weak domains do not extend over the full width of the sample. Furthermore, they are restricted to a range within ≈ 0.5 mm from the cathode border. The movement of these domains corresponds directly to the sinoidal oscillations of the total current signal. As the weak domains can be detected visually even before the current oscillations exceed the noise level, we define V_{c1} as the applied voltage just below their onset.

iii. At a second critical voltage V_{c2}, the oscillations sharply change into a pulse-like shape, the amplitude now covering up to 95 % of the total signal. These oscillations coincide with a distinct domain formation over the whole width of the cathode. The domains drift towards the anode where they vanish and the cycle starts again. In analogy to V_{c1}, we define V_{c2} as the applied voltage just below the onset of these large domains.

iv. Finally, at very high voltages, the total current rises more than three orders of magnitude, indicating the electric breakdown of the sample. As this causes severe damage to the original properties of the sample, this fourth regime was generally avoided.

Even at this early stage of experimentation the advantages of our setup are evident since the video-screen gives clear evidence of *two* critical fields instead of the single one assumed up to now.

4.2 Topology of Domains

We proceed with a qualitative experiment on the topological aspects of high-field domains which develop in the regime (iii) of the $j(E)$-characteristic. Here, the influence of the geometry of the sample on the shape of domains and of the corresponding current pulses is investigated.

Sample A had two parallel bar-shaped In-contacts with a spacing of 6 mm. The circular contacts of sample B were formed by two droplets of In ($\o \approx$ 1.2 mm) placed 2 mm apart from each other; both samples were annealed similarly.

The $I(V_{appl})$-characteristics of samples A and B (Figure 4.2) are quite simi-

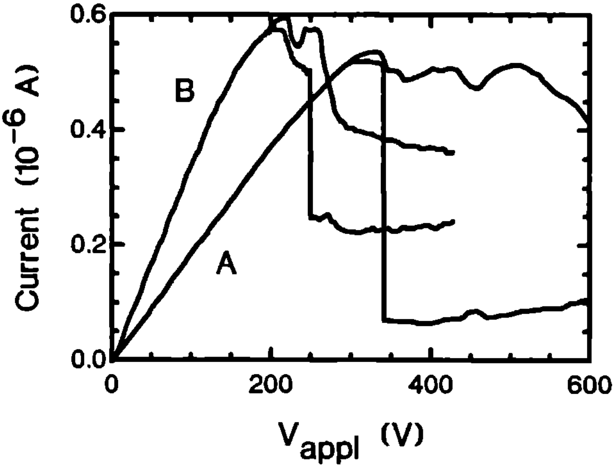

Figure 4.2:
$I(V_{appl})$-characteristics (maximum and minimum current) of a sample with parallel (A) and circular (B) contacts

lar and show both the features described in Section 4.1. The difference between the samples becomes more clear by observing the time-dependent current signal at a fixed V_{appl} in the regime (iii) of large oscillations. The $I(t)$-curves are pulse-like for both samples (Figure 4.3), but sample A oscillates between two distinct levels of current whereas sample B produces a saw-tooth oscillation.

To understand these differences, we employed a transmissive electrooptic setup (Section 3.3) which gives purely qualitative pictures of the domains (Appendix A). For each sample, we took several frames during a complete current cycle at the voltages corresponding to Figure 4.3 ($V_{appl} = 970$ V for sample A, $V_{appl} = 500$ V for sample B).

The Figures 4.4 and 4.5 reveal that the low current level of sample A corresponds to the presence of a planar domain moving from the cathode to the anode. The movement is of constant velocity and the shape of the domain

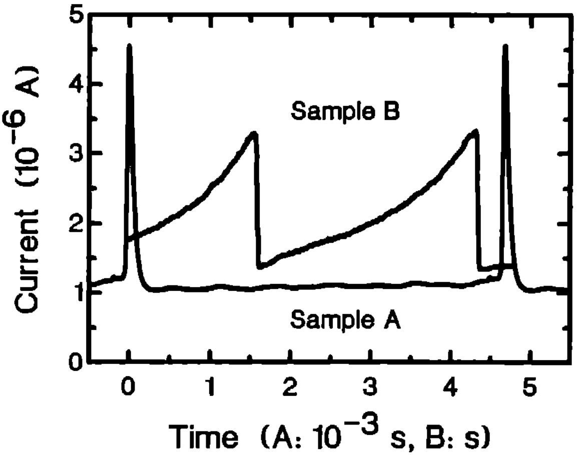

Figure 4.3:
$I(t)$ at a fixed V_{appl} for a sample with parallel (A) and circular (B) contacts. Both samples are operated in the pulse-like regime. The time scale of sample B is divided by a factor 300.

does not change during transit. The current peak occurs during the period where no domain can be seen; this part of the cycle will be closely investigated in the next section. The domain obviously represents a high resistance which reduces the current during its existence.

The same experiment on sample B (Fig. 4.7 and 4.6) shows a significantly different picture. Here, the domain is ring-shaped around the cathode. The movement of the domain corresponds to an increase of the radius of this ring of constant width and no preferential direction towards the anode can be seen. The movement is not constant in time but slightly accelerated. Having reached a certain maximum radius r_{max}, the domain collapses and a new domain is nucleated around the cathode. The current cycle shows a rising signal during the motion of the domain and the current peak occurs on the collapse of the old and the nucleation of the new domain.

The different topologies of the domains become clear if one looks at the mechanism of domain formation. If the sample is biased into the unstable region of the $j(E)$-characteristic, any small, local variation of E will start to grow in amplitude and form a domain perpendicular to the direction of the current (that is, along the equipotentials). Close to a circular contact, the field distribution of a dielectric is radial (Fig. 4.8) and provides the initial local variation of E as a geometrical enhancement. The nucleation of the domain along the equipotentials produces ring-shaped domains as pictured by Fig. 4.6.

The observation that the domain remains ring-shaped even far from the contact implies that its circumference still forms an equipotential line. This can be only explained by the assumption that almost all the applied voltage drops across the domain, leaving the area of the sample outside the ring on a low homogeneous potential in respect to the anode. The direction of j between cathode and the domain's outer circumference remains radial so that the domain represents a stable topological structure which does not change the shape during its motion.

Looking at Figures 4.5 and 4.6, we can suppose that the domain does not change its cross-section significantly during its motion as the intensity and the extension of the sample's surface distortion remain the same. Drawing the simplified picture that a domain can be principally described as a region of high resistance, the current density through the domain is determined by its peak electric field E_{peak}. Therefore, as the domain of sample A stays constant in its extensions during transit, the total current remains on a constant low level. For sample B, the total current through the sample has to increase linearly with the radius of the domain because we have to integrate j over the circumference. Taking into account the accelerated motion of the domain, the total current has to increase superlinearly in time, as it is observed in Fig. 4.7. The observation that these domains collapse at some point will be discussed later on.

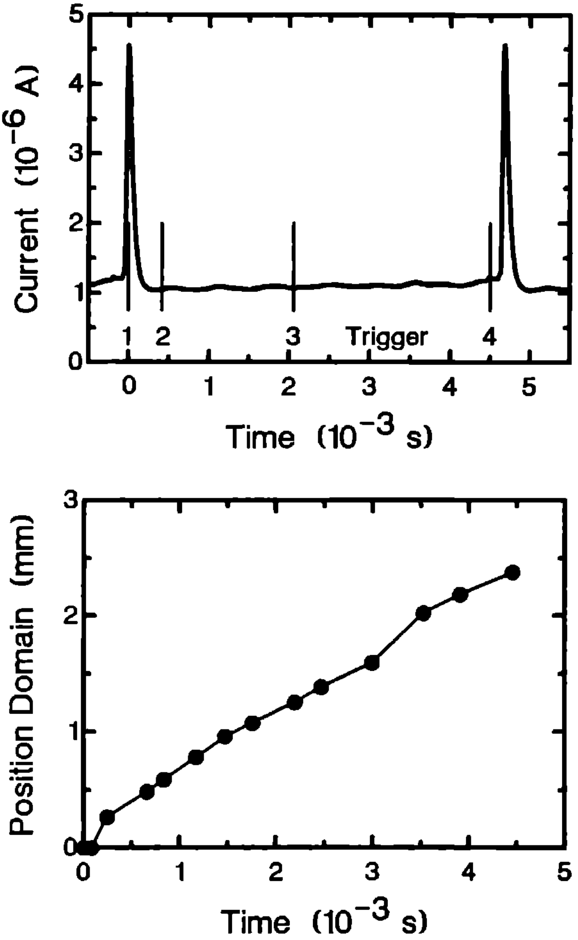

Figure 4.4 :

$I(t)$ and domain position at discrete times for sample A (parallel contacts)

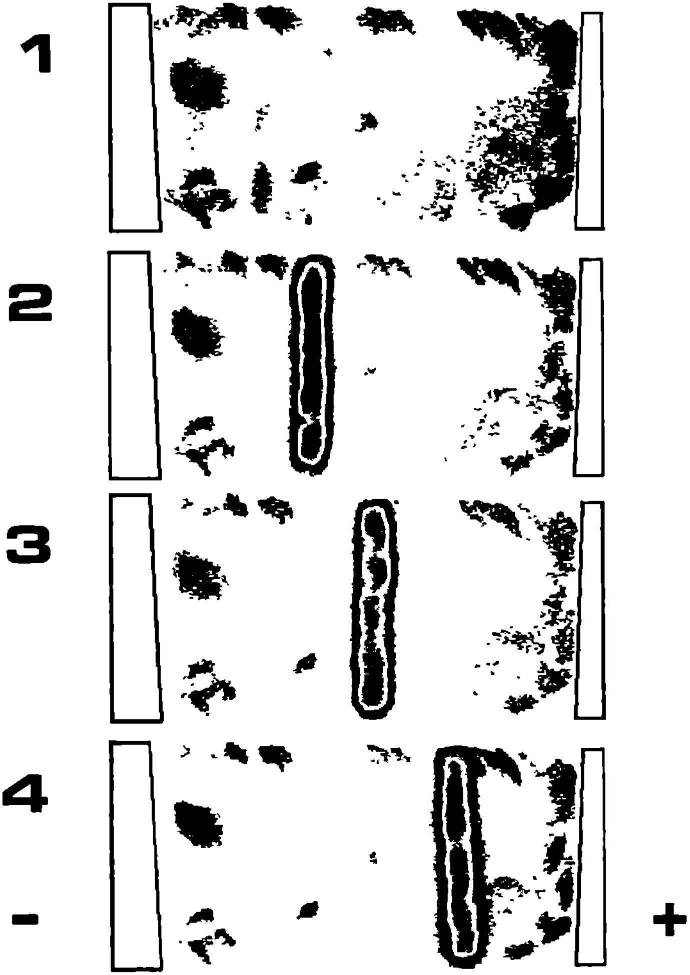

Figure 4.5 : *Domain topology of sample A*

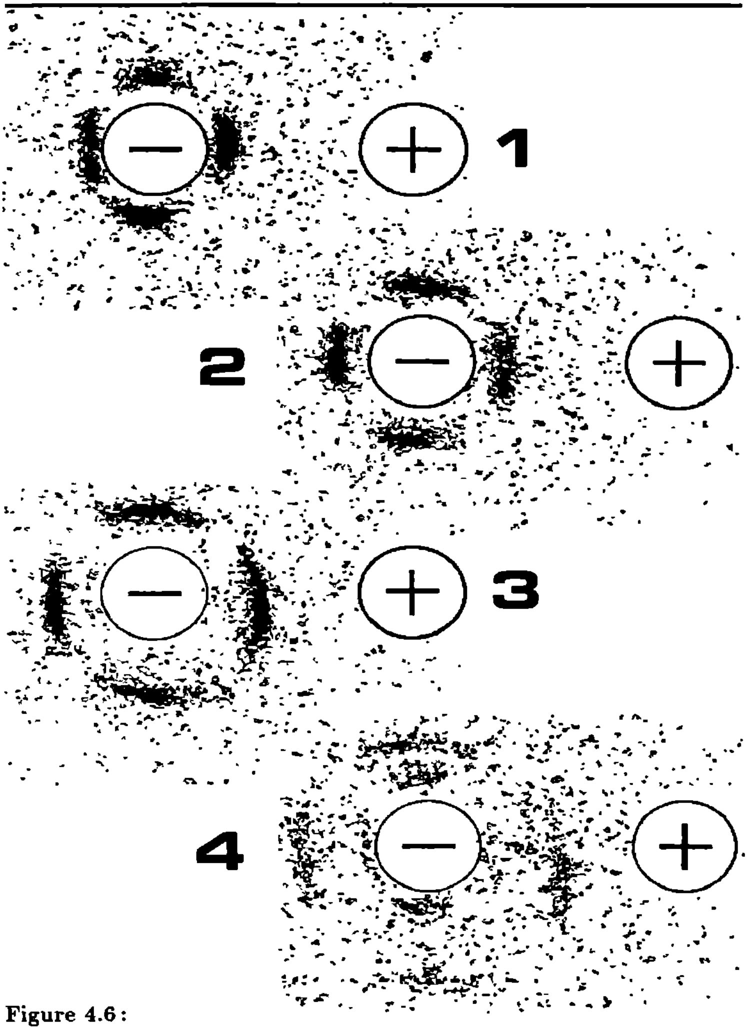

Figure 4.6:

Domain topology of sample B. The fourfold symmetry around the cathode is due to a $\sin^2$*-term in the angular sensitivity of the setup and rotates with the polarization vector of the light in respect to the sample.*

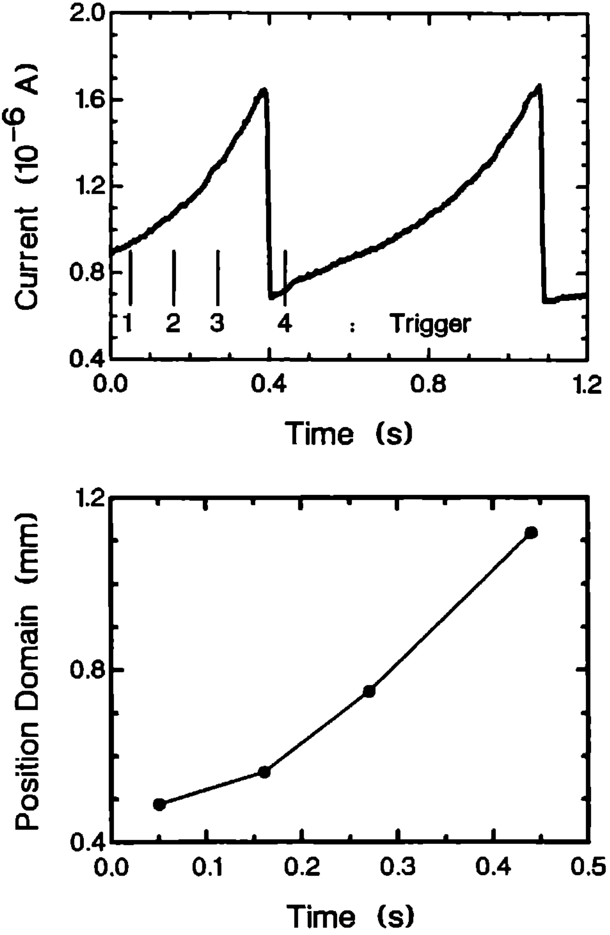

Figure 4.7 :

$I(t)$ and domain position at discrete times for sample B (circular contacts)

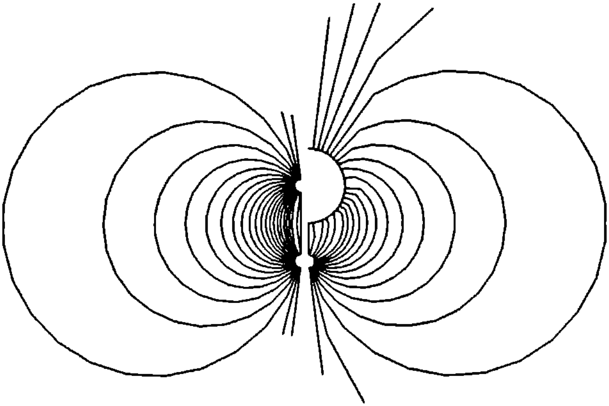

Figure 4.8 :
Field distribution of circular contacts on a dielectric. Left: Initial geometrical enhancement near the contacts. Right: The field and current density remain radial in the vicinity of the outer circumference of the domain (sketched by the upper circle).

4.3 Critical Fields and Temporal Evolution of Domain Cycles

So far, we have employed only qualitative recordings of our camera. Using the possibility of measuring the absolute voltages we also obtain the local critical fields, which has never been done before. This allows us to explain in detail the overall electric behaviour of a sample during a cycle of oscillation.

4.3.1 Critical Fields

The crucial parameter for nonlinear transport is the critical field E_{crit}, upon which the nonlinearity sets in. Experimentally, E_{crit} has been deduced in the past by taking the critical applied voltage V_{crit} at which any oscillation appears and dividing it by the contact spacing L. The fact that E_{crit} for slow domains has been determined to be well below the threshold field for Gunn effect ($E_{c,Gunn} = 3.1 \cdot 10^5\,\mathrm{V/m}$) has led to the development of an alternative model based on localized traps [43] [8] [7]. Obviously, this so-called configurational electric field $E_{conf} = V_{crit}/L$ does not take into account the depletion layer created by any contact in a semiconductor and the resulting distortion of an applied electric field. Lusakowski [41], Sacks [7] and Ridley [33] explicitly point to this problem but, as no spatially resolved measurement of electric fields was possible at that time, they also worked with the assumption $E_{crit} = E_{conf}$.

We can directly measure the detailed voltage distribution and deduce the local electric fields. To investigate the observation of two critical voltages in Sec. 4.1, we recorded the voltage distributions near the cathode of various samples at V_{c1} (onset of sinoidal oscillations) and V_{c2} (nucleation of large domains). All samples had a bar-shaped geometry with parallel contacts which were evaporated with Au, Au/Ge:Ni or Sn to create different Schottky contacts; the two contacts of each sample were mutually operated as the cathode.

The electric fields were deduced (Fig. 4.9) by fitting the measured voltage profiles with an appropriate smooth function and calculating $E(x) = \frac{d}{dx}V(x)$. The critical fields E_{c1} and E_{c2} were taken as the maximum deduced fields in the current direction at the voltages V_{c1} and V_{c2}, respectively. Figure 4.10 shows these values against the corresponding configurational field E_{conf}, thus normalizing the lengths of the different samples and comparing them to E_{conf} (indicated by the line $E = E_{conf}$).

In all cases E_{conf} underestimates E_{c1} significantly because a large portion of V_{appl} drops over the cathode region. Especially for E_{c2} we see that E_{conf} is of no meaning at all. Furthermore, E_{c1} and E_{c2} obviously form two separate regions of electric field. Weak domains set in at $E_{c1} = 0.5\,..\,1.25 \cdot 10^5\,\mathrm{V/m}$ which is the range put forward by the model of field-enhanced trapping. Large domains need critical fields of $E_{c2} = 3.1\,..\,8.8 \cdot 10^5\,\mathrm{V/m}$ which are sufficiently high to accelerate free electrons from the Γ to the L minimums of the conduction band by the Gunn effect.

Another important feature of Figure 4.10 is that there is apparently no link between the contact material of a sample and its values of E_{c1} and E_{c2}. Only the not-annealed Sn-contacts, which are not supposed to have an extended contact region, do not show any weak domains below E_{c2}. This observation implies that in order to study the dynamics of stable domains, the material used for the contacts is irrelevant and a suitable contact method can be used.

The different ranges of critical fields can be explained straightforward by a partition of the sample into two subsystems, i.e. contact region and bulk GaAs. Both of them show a N-shaped $j(E)$-characteristic allowing formation of domains, with the critical field of the cathode N-shaped regime being sub-

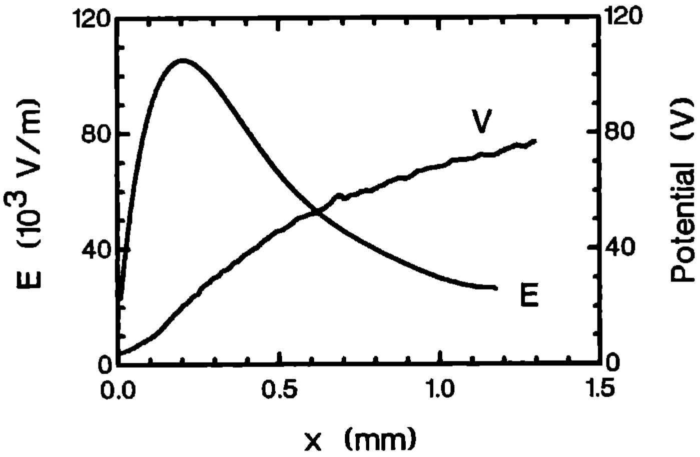

Figure 4.9 :

Measured voltage drop (V) and electric field (E) in the vicinity of the cathode ($x = 0$ mm). The sample is operated below V_{c1} in the stable regime (i). The anode is located at $x = 6.45$ mm, $V_{appl} = 270$ V.

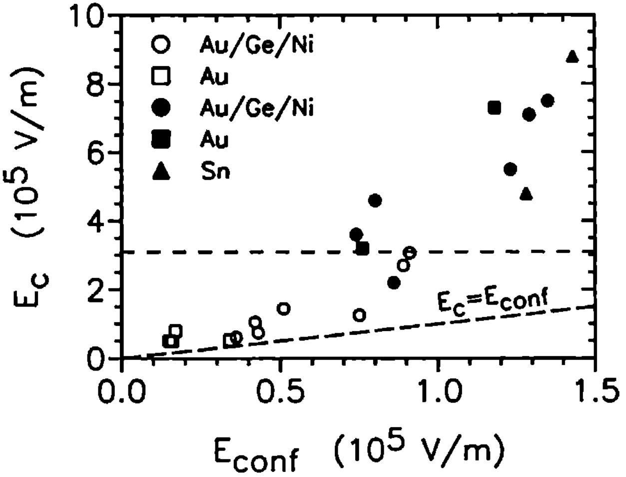

Figure 4.10:

Comparison between critical fields E_{ci} deduced at V_{ci} for various contacts of different materials (the two contacts of a sample mutually acting as a cathode) and the assumption of the according uniform configurational field ($E_{ci} = E_{conf} = V_{ci}/L$, L: contact spacing). Open dots indicate the onset of local weak domains at E_{c1}, full dots the nucleation of bulk domains at E_{c2}. The dotted horizontal line refers to the critical field for Gunn effect.

stantially lower than the one of the bulk. As soon as E_{c1} is reached somewhere at the cathode, weak domains can form at these points. These domains cannot propagate into the bulk GaAs because their fields are too low to nucleate stable domains. Because they are of small lateral extension, they change the current density only locally and thus produce small, sinoidal oscillations in the total current.

By increasing V_{appl}, E_{c2} is eventually reached and a large, stable domain can form over the whole width of the cathode. The current density has to adjust over the whole cross-section of the sample to the field of this domain (which is much higher than the initial E_{c2}) and the total current therefore shows a large amplitude of oscillation.

4.3.2 Domain Cycle

The discovery of the sample's partition into its subsystems - bulk GaAs and contact regions - directly leads to the question how these systems interact during a complete cycle of stable domain propagation. To investigate this question, we operated a bar-shaped sample with parallel Au/Ge:Ni contacts of $L = 6.45\,\mathrm{mm}$ at a fixed V_{appl} in the regime (iii) of pulse-like oscillations. Triggering the camera via a delay line on these pulses, we recorded several voltage distributions at subsequent times of the domain cycle. The width of the camera's exposure window ($\Delta t = 50\,\mu s$) was small compared to the drift velocity of the domain ($v_D \approx 1.6 \cdot 10^{-2}\,\mathrm{m/s}$), so that the movement of the domain had no influence on the determination of fields.

Figure 4.11 shows a cycle of the the current signal for the sample operated at $V_{appl} = 1000\,\mathrm{V}$. The field distributions according to the positions of the exposure window are shown in the insert. The domain with a peak field $E_{peak} \approx 12 \cdot 10^5\,\mathrm{V/m}$ moves as a soliton through the bulk while the current remains at its constant low level. At certain locations of the sample, some parts of the domain change their shape slightly but re-adjust later on. This is in good agreement with Johnson et al. [16] [15] who report an interaction of the domain with dislocation structures within the bulk sample. The small amount of ripple which is seen on the low level signal is probably also due to this interaction because the residual noise of the electric circuit is far below this amplitude.

Figure 4.12 is a close-up on the current peak of the same oscillation as Fig. 4.11. It shows the simultaneous evolution of the maximum detected fields at the anode and the cathode in respect to the current signal. The fast rise of the latter within $\approx 10^{-3}\,\mathrm{s}$ to its peak value is connected to the arrival of the peak domain field at the anode. In the following, the domain remains stationary at the anode whereas its field decays slowly. The loss of electric field is directly transferred to the cathode region without changing the field across the bulk part of the sample. In fact, an intermediate state of the sample with an uniform field distribution of $E_{conf} = V_{appl}/L$, as usually assumed to be connected to the current peak, does not exist at all. Instead, the current signal decays slowly with the electric field at the anode.

As soon as the newly nucleated domain at the cathode exceeds the critical field E_{c2}, it starts to penetrate into the bulk which in turn is accompanied by a rapid drop of the current (within $\approx 10^{-2}$ s, dashed line in Fig. 4.12). At this moment, *two* domains exist within the sample: the decaying one at the anode and the propagating one in the bulk (insert of Fig. 4.12). The latter grows during its movement until the first domain has completely disappeared.

The overall electric behaviour of the sample can be understood if we see these results together with the preceding assumption of two different charac-

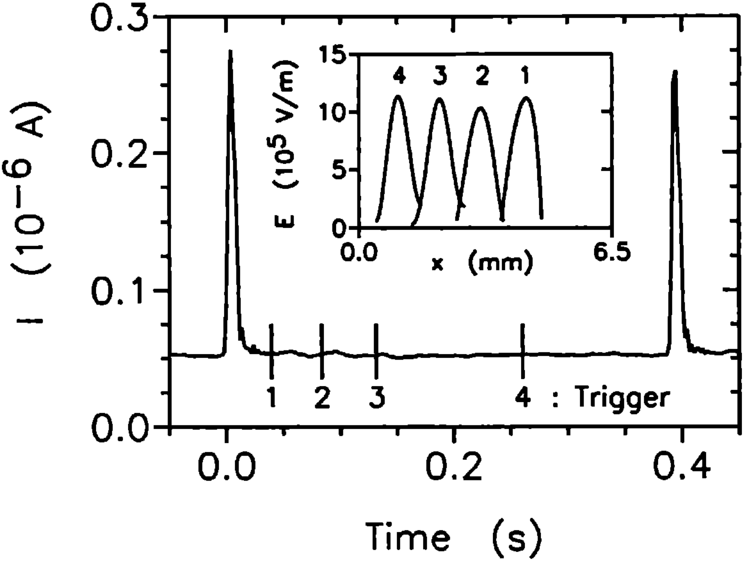

Figure 4.11 :

Current signal in the pulse-like regime (iii) at $V_{appl} = 1000$ V. The insert shows a stable domain with a peak field of $E_{peak} \approx 12 \cdot 10^5$ V/m propagating as a soliton through the bulk (cathode at $x = 6.45$ mm, anode at $x = 0$ mm).

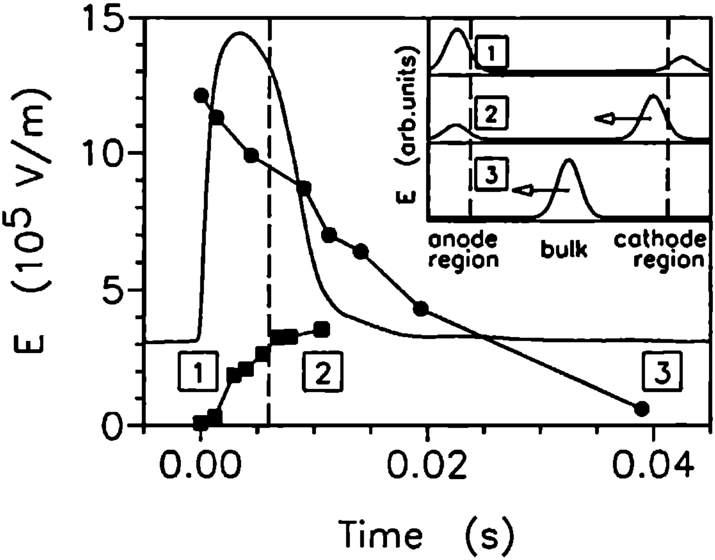

Figure 4.12:

Close-up on the current peak and temporal evolution of the maximum detected fields at the anode (circles) and the cathode (squares) region. The dashed line indicates the observed start of the second domain's movement. The insert sketches the field distribution $E(x)$ corresponding to the times 1,2,3.

teristics $j(E)|_{contact}$ and $j(E)|_{bulk}$ which are both sketched in Figure 4.13. At low applied voltages, all parts of the sample are stable. For higher voltages, E_{c1} is reached somewhere at the cathode; weak domains can form and move within the cathode region whereas the bulk sample remains stable. Finally, a stable domain can form on E_{c2}. As soon as it enters the bulk, the current density has to adjust to a value corresponding to E_{peak} of the domain on $j(E)|_{bulk}$. The contacts are now left under low electric field and are therefore stable. We can neglect their contribution; the behaviour of the sample is governed by

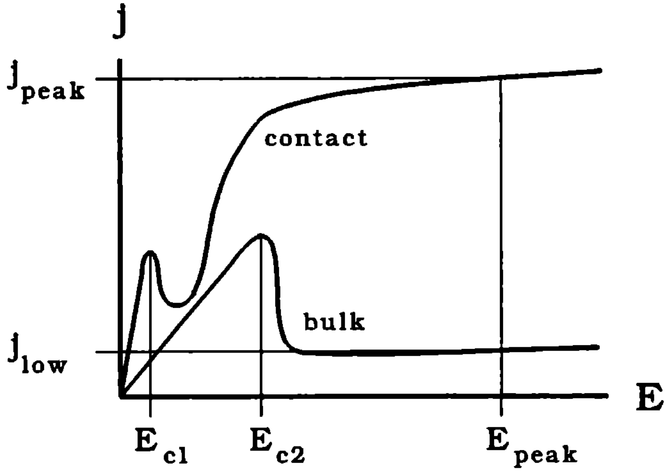

Figure 4.13:
Sketch of the two different $j(E)$-characteristics of the subsystems bulk sample and contact region

$j(E)|_{bulk}$ and we can take the domain principally as a region of high resistance (low total current for high V_{appl}).

When the domain reaches the anode, it imposes its high peak field ($E_{peak} \approx 12 \cdot 10^5$ V/m, Fig. 4.12) to the anode region. Although the $j(E)$-characteristic of this region should differ somewhat from the one of the cathode region, the preceding section nevertheless implies that it has a similarly low E_{c1} compared to the bulk. We therefore conclude that the anode breaks down and can deliver a high current according to $j = j(E_{peak})|_{contact}$. As the domain decays slowly, the current decays also slowly along $j(E)|_{contact}$. The decayed field is directly transferred to the cathode region, leaving the bulk sample under stable low field condition. During this part of the cycle, the behaviour of the sample is ruled by the contacts whereas the contribution of the bulk can be neglected. As soon as the newly created domain at the cathode exceeds E_{c2}, it enters the bulk sample and the current has to adjust rapidly to $j = j(E_{peak})|_{bulk}$. The current reaches its lowest value when the old domain has completely disappeared and the new one has reached its full size.

To sum up, the cycle of one current oscillation is due to the switching of the sample under the movement of the domain between the states "unstable bulk/stable contacts" and "stable bulk/unstable contacts". The assumption that the sample oscillates between $j(E_{peak})$ and $j(E_{conf})$ of the bulk's characteristic as mentioned by other authors [7] [31] is not correct.

The temporal evolution of a complete domain cycle can be described by two characteristic times. t_1 is the decay time of the domain at the anode while t_2 is the time a domain takes for transit through the sample. t_1 determines the duration of the current peak since the current will only drop if the first domain has decayed sufficiently to allow the next domain to enter the bulk. t_2 measures the interval between two current pulses; it is determined by the (constant) velocity of the domain (see Sec. 4.2). As long as $t_1 \ll t_2$, the two states described above do not interfere and the period of oscillation is $t_1 + t_2$. If t_1 approaches t_2, the new domain grows during a part of its motion as it does the one of Fig. 4.12. This eventually leads to the situation that the two domains can interfere with each other. To approach this scenario quantitatively, one can model an idealized cycle on the assumption that the peak field value E_{anod} at the anode is given by an exponential decay of the peak field $E_{dom(n)}$ of the just arrived domain (Fig. 4.14a)

$$E_{anod}(t) = E_{dom(n)} e^{-\frac{t}{t_1}} \tag{4.1}$$

The decayed field is directly transferred to the cathode where the peak of the thus nucleating next domain therefore grows with

$$E_{dom(n+1)}(t) = E_{dom(n)}(1 - e^{-\frac{t}{t_1}}) \tag{4.2}$$

The current is given by $j(E_{anod})|_{contact}$ as long as $E_{dom(n+1)} \leq E_{c2}$. For $E_{dom(n+1)} = E_{c2}$, the new domain penetrates into the bulk which happens at the time t_s :

$$t_s = -t_1 ln(1 - \frac{E_{c2}}{E_{dom(n)}}) \tag{4.3}$$

From this point, the current is determined by $j(E_{dom(n+1)})|_{bulk}$ until the second domain reaches the anode at the time $t = t_s + t_2$ and the current switches back to to characteristic of the contact (Fig. 4.14b). The amplitude of the second domain upon its arrival in respect to the first one is given by

$$\frac{E_{dom(n+1)}}{E_{dom(n)}} = 1 - (1 - \frac{E_{c2}}{E_{dom(n)}})e^{-\frac{t_2}{t_1}} \tag{4.4}$$

where $t_2 = L/v_D$. For $t_2 \approx t_1$, which is the case for high V_{appl} (Sec. 4.4), the second domain collides with the not yet vanished first domain at the anode. This collision cannot be expected to be a linear superposition because both domains consist of charge dipoles and the positive leading edge of the second domain will reach the negative trailing edge of the first one (Fig. 4.15). Two effects of this collision are possible: Firstly, the interaction of the domains may significantly change the decay time t_1 for the second domain. Secondly, the

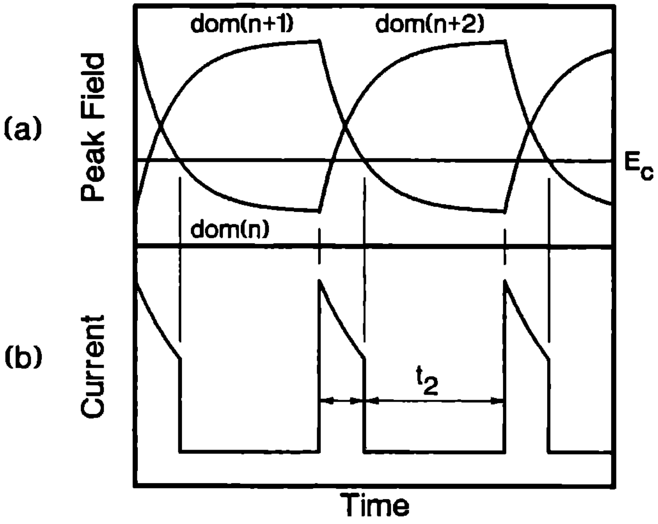

Figure 4.14 :
Sketch of an idealized domain cycle: Peak electric fields (a) and current (b)

domains may partly cancel each other (without changing t_1) so that for the next cycle $E_{dom(n)}$ is changed. Both possibilities lead to the fundamental property of eq. 4.4 that the ratio$E_{dom(n+1)}/E_{dom(n)}$ and therefore $j_{peak(n+1)}/j_{peak(n)}$ can alternate for successive cycles. Allegorically spoken, each domain "remembers" the preceding one which is exactly the feature of recursive mapping, namely $x_{n+1} = f(x_n)$.

Having shown that the current oscillation consists of a nonlinear coupling between the two oscillatory systems bulk GaAs and contact region, an interesting speculation is that one should be able to connect a set of control parameters like t_1, t_2 to the observation of chaotic behaviour of the sample (Fig. 4.16) [44] [13] [9] [11] [10] [45] [46] [42].

With the results of this section, we now return to the ring-shaped domains of Sec. 4.2 and discuss why they collapse before reaching the anode. Figure 4.17 shows the radial distance r_{max} between cathode border and domain at the

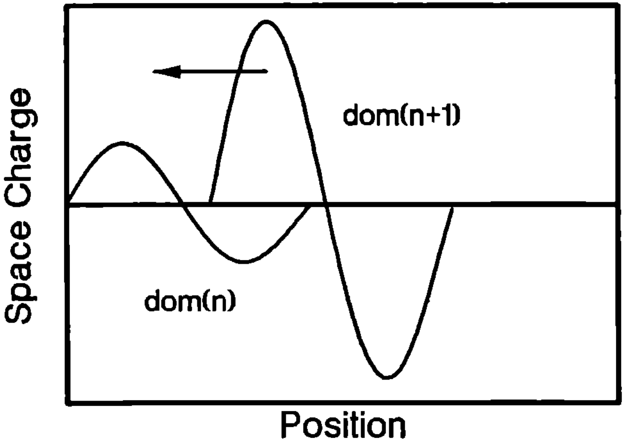

Figure 4.15 : *Sketch of the collision of two subsequent domains at the anode*

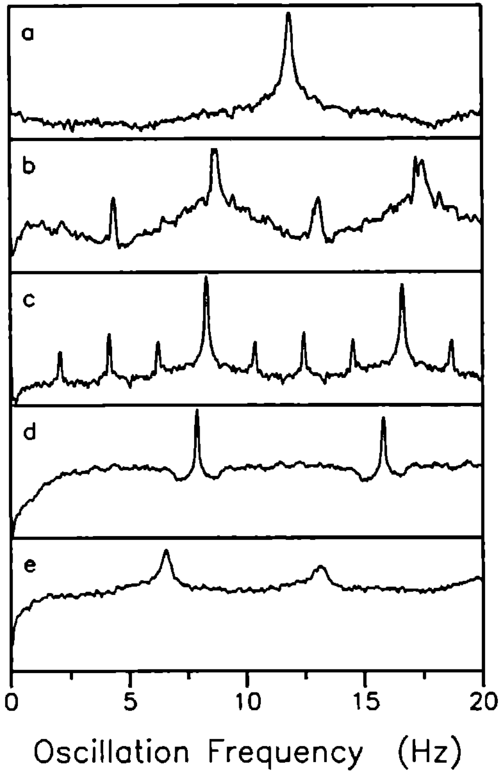

Figure 4.16 :

Frequencies of oscillation in the pulse-like regime (iii). With increasing applied voltage from (a) to (e), the sample shows period doubling (subharmonic in (b), second subharmonic in (c)), the subharmonics become noisy in (d) and the sample exhibits chaotic oscillations in (e). The coordinates are from -110 dBV to -30 dBV each.

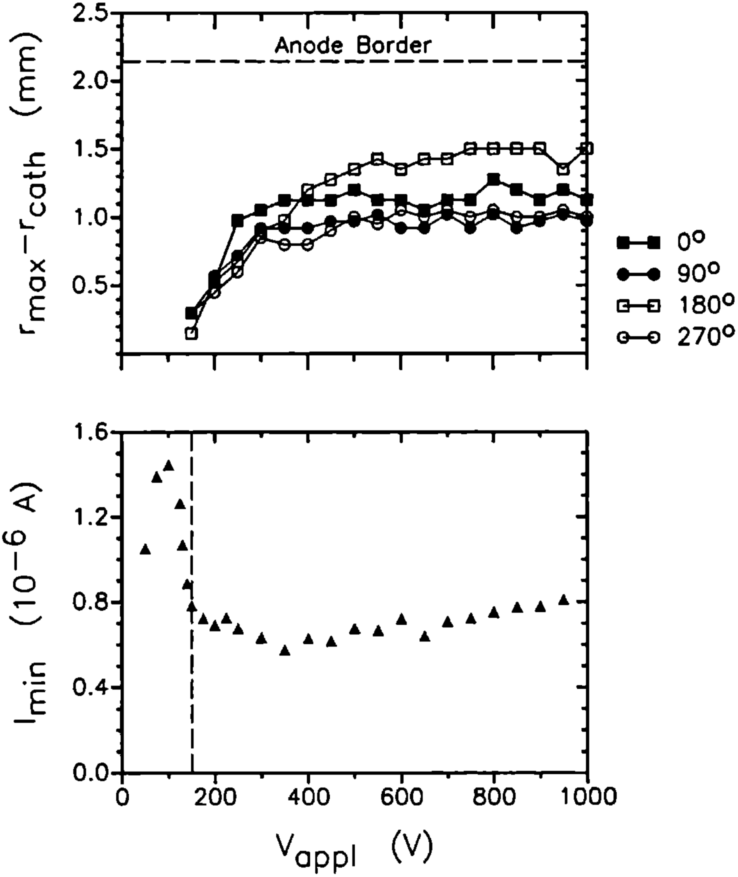

Figure 4.17 : $r_{max}(V_{appl})$ *and* $I_{min}(V_{appl})$ *for sample B (circular contacts)*

moment of collapse for $V_{appl} = 150..1000\,\mathrm{V}$. It can be seen that r_{max} raises with low V_{appl} and reaches a constant value for $V_{appl} \approx 350\,\mathrm{V}$. If we stay in the picture of a high resistive domain, the total current through the sample increases with the radius of the domain. Thus, as the radius of the cathode is constant, a rise of the total current implies an increase of the current density at the cathode. Due to the N-shape of the $j(E)$-curve, a j_{max} exists which cannot be exceeded. When this j_{max} is reached at the cathode, the domain cannot move further while conserving its shape as there is no current available to feed this movement. It therefore has to fade out at r_{max} which in return enhances the field at the cathode. Since the cathode region already is at the border of stability marked by j_{max}, the enhancement of the field pushes it into instability. A new domain is created which causes the current density to drop again to the low value and the cycle starts again.

Supposing that at $V_{appl} < 350\,\mathrm{V}$ a domain has not yet reached an E_{peak} corresponding to the minimum of $j(E)$ (Fig. 4.17), j_{max} will be reached at a lower value of r_{max} because j at the cathode starts to increase from an already higher value. If E_{peak} increases with V_{appl}, the starting value of j will decrease allowing in turn the domain to increase r_{max}. This radius has to remain constant as soon as the initial domain imposes $j_{min}(E)$. Accordingly, Figure 4.17 reveals that the minimum of the initial total current (which is proportional to $j|_{cathode}$) is reached at about the same V_{appl} as r_{max} becomes constant.

4.4 Stable Domain Propagation

So far having studied the overall nonlinear behaviour of the coupled system bulk GaAs/contact regions, we now concentrate on stable domains propagating through the bulk. As the results of the preceding sections have shown, we can neglect here the contribution of the contacts because they are subjected to linear low-field conditions so that we have directly access to bulk properties.

We first establish a control parameter for domains which is independent of the sample's size. Next, we study the development of the growth and the shape of domains as function of the increasing control parameter, which enables us to decide on the general shape of the $j(E)$-characteristic as well as on the origin of the involved space charge. However, the most interesting point in the investigation of a nonlinearity is not only to record the resulting phenomena such as critical field, amplitude of the domains, maximum space charge etc, but to understand the mechanism of structure formation for which it is essential to obtain information about the intrinsic properties of the system. In the last section, we therefore investigate the field dependencies of the current density j, the free carrier concentration n_{free} and the capture coefficient c_{EL2} of the traps.

The experiments were performed on three different, bar-shaped samples with contact spacings of $L = 6.45\,\text{mm}$ (A), $L = 4.05\,\text{mm}$ (B) and $L = 4.25\,\text{mm}$ (C). All contacts were alloyed of eutectical Au/Ge containing 6 % Ni, which gave best results in terms of mechanical stability (Sec. 4.1). The samples were held on stabilized room temperature and were shielded against any illumination. The voltage distribution over a sample was measured at a time when the domain was about in the middle of the sample, in order to keep the largest distance from the contacts. Because of the synchronous exposure technique, the domains could only be measured within a range of V_{appl} where the domain cycle τ_{osc} showed no fluctuation during the average. To be able to sort out any residual influence of the cathode on the domains, a domain was measured for every sample and for two directions of V_{appl} so that each contact acts once as the cathode and once as the cathode. Consequently, data is denoted by AL, AR, BL, etc. indicating the actual sample (A,B,C) and cathode (L or R).

Figure 4.18 pictures typical voltage profiles obtained for the two electrical polarizations of sample A. An experimental point consists of the voltage profile together with the corresponding value of the total current. From the profile, we can extract the peak domain field E_{peak}, the field far from the domain E_{out}, the space charge profile $\rho(x)$ and the domain width w. E_{peak} and E_{out} were determined manually by construction of the corresponding tangents. The width of the domain w was found by taking the distance between 10 % and 90 % of the voltage drop over the domain. However, it can bee seen in Fig. 4.18 that in general w is not small compared to the length of the sample. Due to the extended edges of the domain, E_{out} can only be estimated, as the slope of $V(x)$ steadily decreases towards the contacts. A functional dependence of E_{out} on V_{appl} or another parameter is therefore not easy to resolve. However, it can be seen clearly that E_{out} is much smaller than E_{peak}, confirming that the area outside the domain is indeed almost an equipotential plane as already concluded from the ring-shaped domains (Sec. 4.2).

The electric field distribution $E(x)$ was calculated by fitting $V(x)$ with an appropriate smooth function which was then derived for $E(x)$. In a next step the smoothed $E(x)$ was derived for $\rho(x)$. The different values of E_{peak} obtained manually, by the maximum of dV/dx and by integrating $\rho(x)$ all coincided within 5%.

4.4.1 Domain Excess Voltage

The first point of investigation is to establish a control parameter for domains which is independent of a specific sample. V_{appl} cannot be such a parameter, because one has obviously to increase it for a sample of larger contact spacing in order to obtain the same domain size as in a short sample.

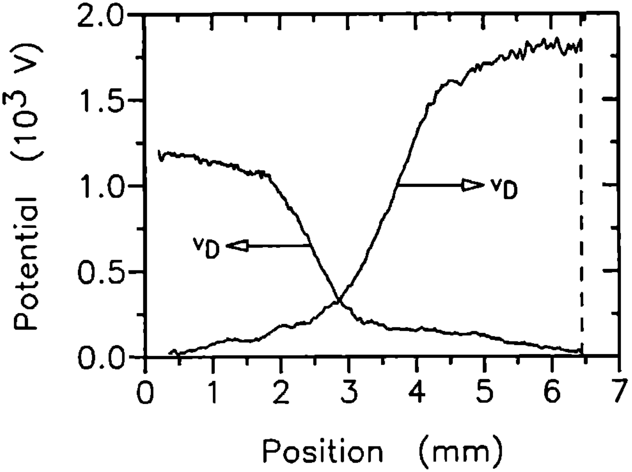

Figure 4.18 :

Typical voltage profiles obtained from sample A for both sides of electrical polarization. The left-hand contact is located at $x = 0$ mm, the right-hand one at $x = 6.45$ mm (indicated by the dashed line)

According to Sacks and Milnes [7] one can instead characterize a domain by an excess voltage V_{exc} which is defined for a finite sample by

$$V_{exc} = \int_{x=0}^{L} (E(x) - E_{out})dx \tag{4.5}$$

and can be approximated as

$$V_{exc} \approx V_{appl} - E_{out}L \tag{4.6}$$

V_{exc} is a normalization of V_{appl} to the sample length, and can be pictured in an $E(x)$-diagram as the area under the electric field of a domain which exceeds the level of E_{out} (Fig. 4.19). It is a simple measure of the overall domain size but it gives no further details on the domain's width or peak field.

We extracted V_{exc} from the voltage profiles by means of the three tangents representing the peak field E_{peak}, the field near the cathode $E_{out}|_{low}$ and near he anode $E_{out}|_{high}$. Due to the large drop of voltage over the domain width in respect to the applied voltage, the contribution of the fields outside the domain to the relative error of V_{exc} was small and $\Delta V_{exc}/V_{exc} \approx 5\,\%$. Using the electric field distribution $E(x)$, V_{exc} was on the other hand calculated numerically by integrating the area of the domain peak. This value was within the error bars of the one manually determined.

The plot of the domain size as a function of the applied voltage $V_{exc}(V_{appl})$ for the samples A, B and C (Fig. 4.20) reveals that in the investigated range $350\,V \leq V_{appl} \leq 2500\,V$ of stable domain cycles, no tendency of the domain size V_{exc} to saturate can be detected. The curves show neither significant differences between the two electric polarizations of each sample nor between different samples. We therefore conclude that V_{exc} reflects a bulk property with no residual contributions of the contacts. Furthermore, it is found that $V_{exc}(V_{appl})$ is the same for all three samples independently of contact spacing or other specific properties. To summarize the above, the characterization of a domain by the parameter V_{exc} is fully justified by our data. It should be emphasized here that this is the first experimental verification of the concept of V_{exc} since our setup is the first one to provide $V(x)$ with sufficient resolution.

From the relation between V_{appl} and V_{exc} we can indirectly gain information about the general shape of the $j(E)$-characteristic. Since V_{appl}, V_{exc} are macroscopic parameters whereas $j(E)$ is a local relation, one can conclude only numerically from $j(E)$ on the domain structure. Sacks and Milnes [7] have

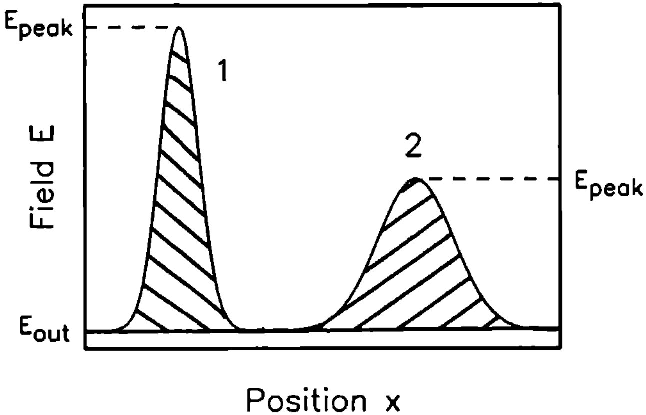

Figure 4.19:

Sketch of $E(x)$ for two domains. The hatched areas represent the domain excess voltages $V_{exc} = V_{appl} - E_{out}L$ and are a measure for the size of the domain. Although domain 1 and 2 have different shapes, their sizes given by V_{exc} are the same.

shown that for a $j(E)$ as pictured in Fig. 2.4 (stable $\frac{dj}{dE} > 0$ for $E = 0 .. E_{crit}$ and unstable $\frac{dj}{dE} < 0$ for all $E > E_{crit}$), an increase of V_{appl} strengthens the spatial structure of the sample: The domain peak field E_{peak} increases and with it the domain size V_{exc}. At the same time, the increase of E_{peak} decreases the current density j because $\frac{dj}{dE} < 0$. The low-field bulk has the same j but $\frac{dj}{dE} > 0$ so that its field E_{out} decreases with j. Sacks and Milnes summarize this behaviour by stating that independently of a specific sample, V_{exc} decreases steadily with increasing E_{out} (Fig. 4.21).

Our experimental determination of E_{out} is too uncertain for a direct comparison of $V_{exc}(E_{out})$ to the theoretical one. Instead, we reconstruct $V_{exc}(E_{out})$,

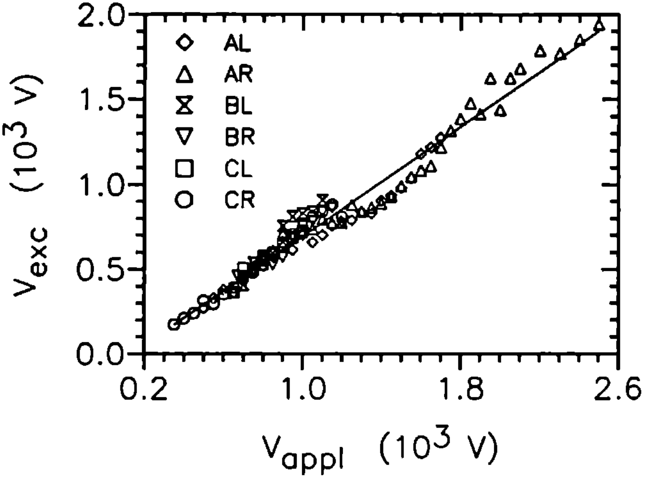

Figure 4.20:
Domain size V_{exc} as a function of the applied voltage V_{appl} for sample A, B and C

using our data $V_{exc}(V_{appl})$ of Fig. 4.20 which can be fitted quite well by

$$V_{exc} = -b_0 + b_1 \cdot V_{appl} \tag{4.7}$$

where b_1 is a parameter determining the size of a domain as a function of the applied voltage. Comparing eq. 4.7 to the definition of V_{exc} (eq. 4.6) gives

$$E_{out} = \frac{b_0}{L} + \frac{1-b_1}{b_1 L}(V_{exc} + b_0) \tag{4.8}$$

Eq. 4.8 shows that b_1 has a critical value, $b_1 = 1$, which determines the shape of $j(E)$: For $b_1 > 1$, E_{out} decreases with increasing V_{exc} and $j(E)$ is formed by a stable low-field and an unstable high-field branch (Fig. 2.4). In the case $b_1 < 1$, E_{out} increases with V_{exc} which cannot be explained by a such characteristic.

Table 4.1 shows the values for b_1 over the investigated range of V_{appl} for the different samples. Obviously, b_1 is a parameter specific to GaAs and not to a particular sample as its values are quite identical. Furthermore, it can be seen that, except for sample B's left contact, b_1 is always below unity with a mean value of all samples of $\overline{b_1} = 0.804$. The $V_{exc}(E_{out})$ reconstructed by eq. 4.8 is shown in Fig. 4.21 and compared to the theoretical one. It is evident that a $V_{exc}(E_{out})$ and thus the $j(E)$-characteristic proposed by Sacks and Milnes does not hold. In contrary to them, our very basic finding is that for an increasing applied voltage both, the domain size and the field far

Sample	AL	AR	BL	BR	CL	CR	A,B,C
b_1	0.7510	0.8437	1.2120	0.9304	0.9257	0.8735	**0.8040**

Table 4.1 :

Values of the structural growth parameter b_1 fitted for different samples

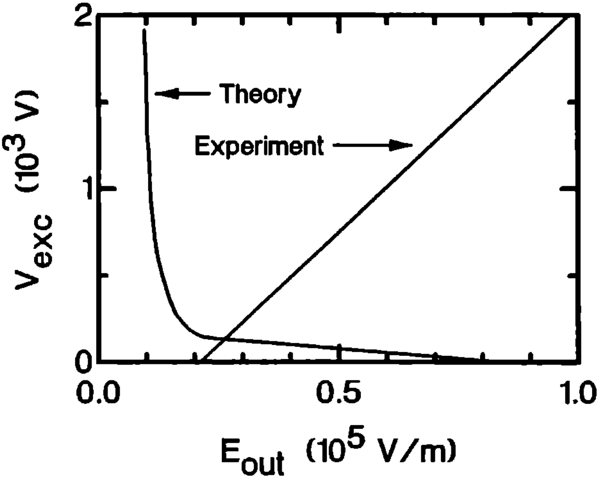

Figure 4.21 :

Comparison between $V_{exc}(E_{out})$ predicted by theory (for a carrier concentrations of $n_0 = 5 \cdot 10^{14}\, m^{-3}$, after Sacks and Milnes [7]) and obtained by our experiment.

from the domain increase. This implies that the low-field regions as well as the domain are operated on stable branches of $j(E)$ which therefore has to be composed within the investigated range of a stable low-field regime, an unstable intermediate regime and a stable high-field branch according to Fig. 2.1b. A domain formation based on such a characteristic corresponds to the Maxwell construction of a phase transition.

4.4.2 Shape of Domains

With V_{exc} as the characteristic parameter to describe domains, we can investigate in detail the evolution of a domain by its size and can thereby obtain information about the origin of the involved space charge. A general observation is that the electric field profile of a domain is symmetrical independently of its size, as already predicted by Sacks and Milnes [7]. Fig. 4.22a shows that E_{peak} grows linearly with V_{exc} up to $V_{exc} \approx 1000\,\mathrm{V}$ where E_{peak} saturates at a value of $E_{peak} \approx 10 \cdot 10^5\,\mathrm{V/m}$. Herefrom it can be concluded, that the total amount of charge (ionized traps and/or free carriers) accumulated in a domain is limited and corresponds to a saturation value of $6 \cdot 10^{15}\,\mathrm{e/m^{-2}}$ times the cross-section of the sample. For a further growth in size, above the saturation limit of V_{exc}, the domain has therefore to change its shape.

From $E(x)$, we determine $\rho(x)$ by differentiation. Fig. 4.22b plots the dipole peak value $|\rho/e|_{max} = (|\rho_{max,-}| + |\rho_{max,+}|)/2e$ as a function of the domain size. After a linear growth with V_{exc}, it reaches is maximum at about the same domain size where E_{peak} saturates. While the domain size (V_{exc}) grows further, $|\rho/e|_{max}$ decreases again linearly and since E_{peak} (or the total charge) stays constant, the domain's width instead of its height increases as shown in Fig. 4.22c. The maximum value of the charge density $\rho \approx 0.8 \cdot 10^{18}\,\mathrm{e/m^{-3}}$ (Fig. 4.22b) is a factor of 10^5 higher than the free carrier concentration. The latter has not increased by a factor of 10^5 since the corresponding decrease in resistivity is not observed. Hence, the space charge of our domains has to be formed exclusively by the localized charge of ionized traps and Fig. 4.22b is a plot of $N_t^-(V_{exc})$. This is a basic difference to Gunn domains, which are entirely formed by modulation of the free carrier concentration and are highly asymmetrical in shape (narrow and huge accumulation layer / broad and shallow depletion layer). On the other hand, there has to be some mechanism which limits the ionization of traps because the total density of the involved

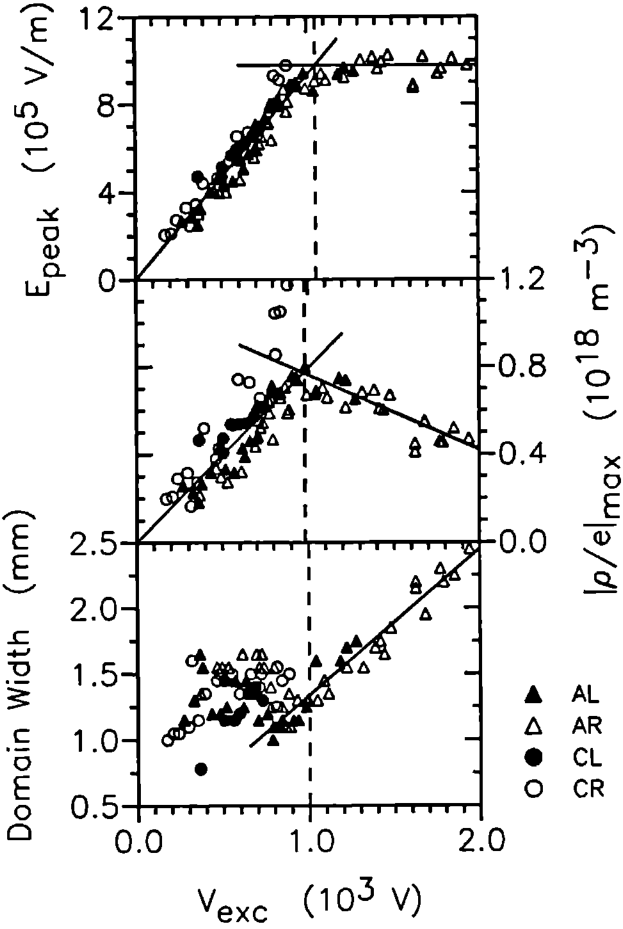

Figure 4.22:

Amplitude E_{peak}, maximum space charge and width of domains as a function of V_{exc} for sample A and C. The lines are drawn to guide the eye.

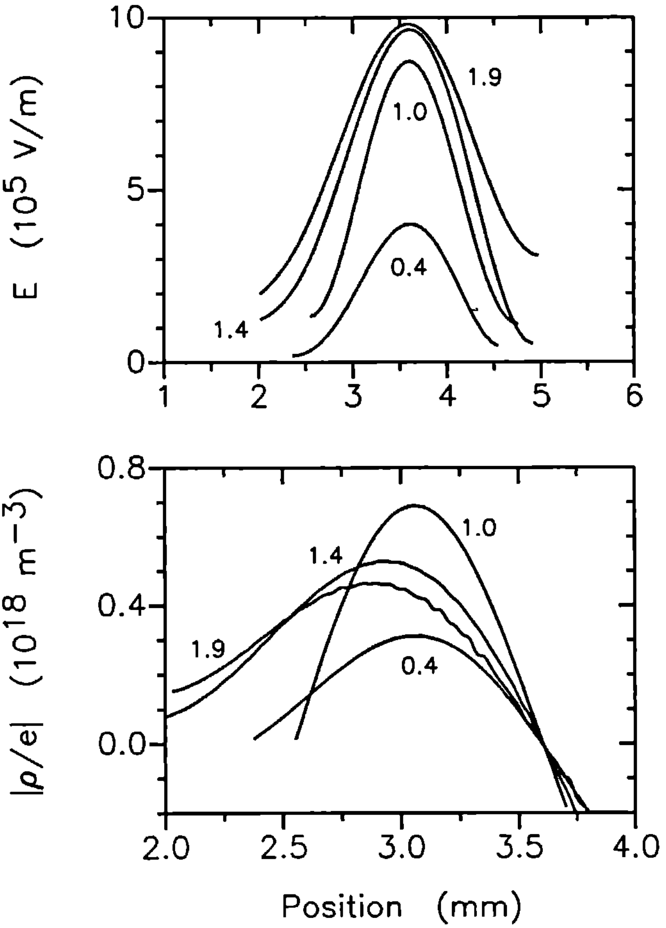

Figure 4.23 :

$E(x)$ (above) and one branch of charge density distribution $\rho(x)$ (below) for sample A at different domain sizes V_{exc} (indicated at the curves in 10^3 V).

midgap trap EL2 is $n_{EL2} = 10^{22}\,\mathrm{m}^{-3}$ whereas the maximum detected charge density corresponds to only 0.01% of this trap density.

To sum up, we can describe the domain growth by the parameter V_{exc} as demonstrated in Fig. 4.23. Below $V_{exc} \approx 1000\,\mathrm{V}$, the domain grows linearly in height because the density of ionized traps increases. Due to the fact that $|\rho/e|_{max}$ (which is a measure for the "steepness" of the domain) also grows linearly, the width of the domain stays almost constant. Above $V_{exc} \approx 1000\,\mathrm{V}$, the totally involved charge stays fixed and the width of the domain is increasing. But since meanwhile the steepness of the domain decreases during growth, the domain does not become flat-topped as predicted by Sacks and Milnes [7] or Ridley and Wisbey [8].

The change in growth behaviour can also be illustrated if one plots the averaged specific resistance of a domain R_{domain} as a function of its size (Fig. 4.24). These values are obtained by dividing V_{exc} by domain width and the observed current density in presence of a domain. One can see that R_{domain} is directly correlated to E_{peak}, growing linearly first and saturating towards bigger domain sizes. It can be concluded that the current through the sample is determined by the properties of the domain and that the low-field bulk only plays a minor role. This is in close agreement with the results of Sec. 4.3 and with the discussion in Sec. 4.4.

4.4.3 Field-Dependent Characteristics

The elementary relation in the discussion of nonlinear transport is the field dependence of the current density $j(E)$. At the same time, the experimental access to $j(E)$ is most difficult because it is a local variable $j = j(x)$. In the case of domain formation, the electric field becomes a local parameter $E = E(x)$ so that in general neither j is represented by the total current I nor is E given by the applied voltage, as it can be assumed for linear transport. The standard $I(V_{appl})$-characteristic (which is all one can measure without a spatially resolved experiment) therefore hides almost all relevant details.

Since we measure the local voltage distribution, we directly have access to $E = E(x)$ and can for the first time establish $j(E)$ experimentally. For this we use the general feature described in Sec. 2.1. During the presence of a stable domain, the sample is operated on two different points of the same $j(E)$-characteristic which are connected by an identical current density. From

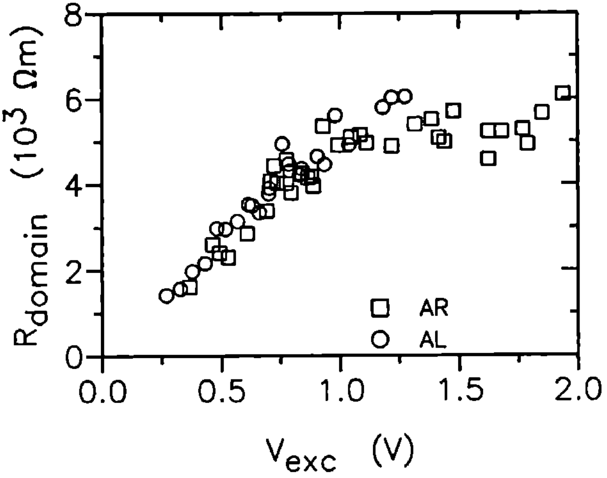

Figure 4.24: *(Averaged) specific resistivity of domains as a function of V_{exc}*

Sec 4 4 1 it already results that these two points are both located on stable branches of $j(E)$ and that $j(E)$ is therefore divided within the interesting region ($0 \le E \le 11 \ 10^5$ V/m) into a low field stable, an intermediate unstable and an high field stable part We know from the discussions of the preceding sections that the current through the sample is ruled by the domain peak field E_{peak} Since the current density directly given by I/A for a rectangular sample of a cross section A must be continuous, it is also connected to the field far from the domain E_{out} and we can construct two stable points of the $j(E)$ characteristic by $(I/A)(E_{peak})$ and $(I/A)(E_{out})$

The third (unstable) point on the characteristic of the same current density cannot be reconstructed and we have no information of the unstable region of $j(E)$ It might be argued that here, relevant information could be obtained from the maximum current I_{peak} arising from the nucleation and annihilation of the domains during a cycle However, our analysis (Sec 4 3 2) showed that this value is determined by the contact and has no relation with bulk properties

Furthermore, we proved that the often assumed state of homogeneous field $E_{conf} = V_{appl}/L$ throughout the sample during the current peak does not exist.

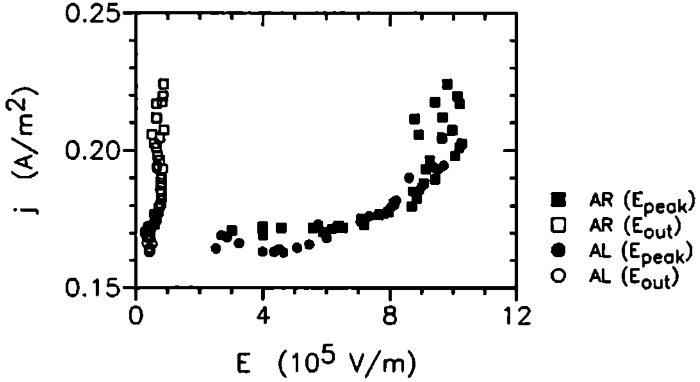

Figure 4.25 : *$j(E)$-characteristic for sample A*

Fig. 4.25 shows as an example the parts of $j(E)$ reconstructed for sample A. It is a new step in the description of slow domains, because it represents the first direct, experimental reconstruction of the real bulk $j(E)$-characteristic of this system so far. Two remarks have to be added to this reconstruction: Firstly, $j(E)$ is a local characteristic which may vary with the defect and impurity concentration across the sample. In our measurements, we took instead the values of E_{peak} and E_{out} on two different locations of the sample. Fig. 4.25 can therefore only be taken as an average of $j(E)$ over the sample. Secondly, the determination of E_{out} is rather difficult, due to the extended width of the domain in respect to the sample length (Sec. 4.4). We therefore have to allow for a reasonable error of at least 50 % in the low-field part of this characteristic. The high-field branch of Fig. 4.25 is quite accurate as the values of E_{peak} are well known and vary only due to the interaction of the domain with dislocation structures in the sample.

The maximum low-field value of the current density in Fig. 4.25 should not be confused with the critical fields directly measured in Sec. 4.3.1. The $j(E)$ presented here includes only points at which the electric field is stable and has to it leave out any parts of the characteristic which are unstable or critical. The fact that the low-field stable part of Fig. 4.25 ends at a field of $E \approx 1.2 .. 2.5 \cdot 10^5$ V/m indicates that at this point the domain cycle became too unstable for our synchronous measurement technique.

Besides the correct description of the structural growth along two stable branches which is the concept for its construction, Fig. 4.25 explains the high-field limits for the existence of domains. With increasing V_{exc}, a medium size domain shows an increasing E_{peak} value without changing its width. Simultaneously, j_{min} and E_{out} increase through $j(E)$ until from a certain point on, an

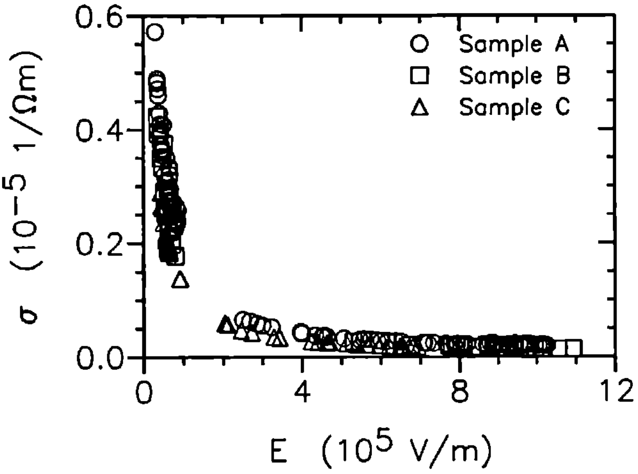

Figure 4.26:

Conductivity σ as a function of the electric field E for the samples A, B and C

increase of V_{exc} cannot increase the peak field anymore. The domain therefore has to increase in width rather than in height. At the same time, we see that the current starts to increase drastically which has to lead to a forced increase of E_{out}. Eventually, the sample reaches a state where even the low-field regions become critical and the sample is now at the edge of stability for domains. Any further increase of V_{exc} causes the low-field region to become unstable, too. Although the details of this second transition are not clear, it is obvious that the overall electric behaviour of the sample will change. This is consistent with our observation that, from this point on, the period of a domain cycle shows big fluctuations.

The next step of our analysis is the successive decomposition of the equation $j(E) = \sigma(E)E$. Fig. 4.26 shows the plot of the conductivity $\sigma(E)$ deduced from $j(E)$ for the three samples. All curves show the same shape and almost the

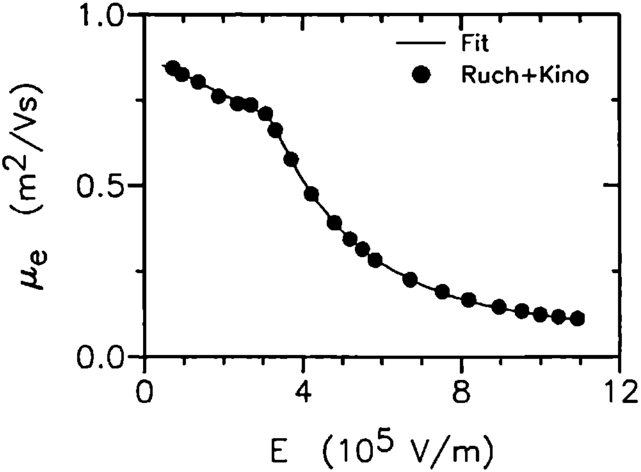

Figure 4.27:
Electron mobilty μ_e in GaAs from measurements by Ruch and Kino (1967)

same absolute value which once again gives evidence that we are measuring the properties of bulk GaAs. The low-field parts can be fitted by a linear function $\sigma(E) = \sigma_0 + \sigma_1 E^{-1}$ with $\sigma_1 \approx 0.12\,\mathrm{V}/\Omega\mathrm{m}^2$. The decrease in conductivity obviously already starts at fields lower than our lowest measurement point of $E = 0.2 \cdot 10^5\,\mathrm{V/m}$. The high-field parts can be fitted quite well by a quadratic function in $(1/E)$ with coefficients of the same order of magnitude as σ_1. We see that the conductivity does not have a minimum at intermediate fields, as it is the case for the current density, but decreases up to the end of the investigated field range.

Finally, we can obtain the free carrier concentration $n_{free}(E)$ from the relation $\sigma(E) = e n_{free}(E)\mu(E)$ by eliminating the carrier mobility $\mu(E)$ using the measurements of the carrier velocity $v(E)$ by Ruch and Kino [47]. The corresponding values of Fig. 4.27 were obtained by calculating $\mu = v/E$ and fitting them by an appropriate function. Fig. 4.28 shows the thus obtained $n_{free}(E)$-characteristics for the samples A, B and C. The absolute value of $n_{free} = O(10^{13}\,\mathrm{m}^{-3})$ is in good agreement with the data provided by the wafer manufacturer. Variations between the different samples are probably due to slight variations of the impurity and trap concentration which is known to change with the position on the wafer. For all samples, the carrier density can be fitted by an expression

$$n_{free}(E) = n_0 \cdot e^{-a(\frac{E-b}{E_0})^c} + 0.1(E/E_0)^d \qquad [E] = V/m \tag{4.9}$$

where $n_0 = 3\,..\,5.7 \cdot 10^{13}\,\mathrm{m}^{-3}$, $E_0 = 1 \cdot 10^5\,\mathrm{V/m}$, $a = 1.5\,..\,1.8$ and $b = 0.1\,..\,0.35 \cdot 10^5\,\mathrm{V/m}$. The exponents are $c = 0.75\,..\,0.9$ and $d = 0.7\,..\,1$. Principally, n_{free} decreases almost exponentially for fields below $1 \cdot 10^5\,\mathrm{V/m}$ to reach a minimum around $E = 3 \cdot 10^5\,\mathrm{V/m}$. This exponential decrease is consistent with a trapping mechanism over a repulsive barrier. Above this field, n_{free} increases linearly with field. This behaviour implies that the traps have their highest capture coefficient at the minimum of n_{free}, because the capture by traps is the only mechanism affecting the carrier density.

The low-field results are a dramatic demonstration of the field-enhanced trapping mechanism. The data show directly that, below a certain field, the carrier density *decreases* with increasing field. This observation is quite unlikely if one thinks rather of carrier multiplication through impact ionization. Also the fact that at even higher fields the density starts to increase again, is entirely new. This - intuitively more acceptable - result is probably caused by an enhanced ionization of trapped carriers which eventually will lead at very high fields to a destructive mechanism by the final breakdown.

To obtain further insight, we calculate the free carrier profile of a domain using the field profile deduced from the measured $V(x)$. Any field anywhere in the sample must correspond to a local free carrier density which can be obtained from the fits of n_{free} as a function of E. Fig. 4.29 shows such a profile $n_{free}(x)$ of a domain ($V_{exc} = 1000\,\mathrm{V}$), together with $E(x)$ and the distribution of ionized traps $N_t^-(x)$ which is equivalent to the space charge ρ/e and derived from $E(x)$. We see that the free carrier profile has a distinct "w"-shape with a ratio of $n_0/n_{min} \approx 4$. Accordingly to the fit $n_{free}(E)$, the position of n_{min} corresponds to a field of $E \approx 3 \cdot 10^5\,\mathrm{V/m}$. As this feature is observed for all domains recorded during this experiment, it confirms the suggestion that the capture coefficient of the traps should be highest at $E \approx 3 \cdot 10^5\,\mathrm{V/m}$. Towards the center of the domain, n_{free} recovers to about $1/2 \cdot n_0$ which is much more than calculated by Sacks and Milnes. This means that the charge dipole forming the domain is accompanied by two separated depletion regions of free carriers, whereby the junction represents an almost low-field concentration of carriers. Although the space charge integrated over the whole sample is zero, we can see clearly that a domain represents electronic transport where the local charge neutrality is not given.

We can summarize all information obtained in this section in order to conclude on the field dependence of the capture coefficient of the trap EL2 $c_{EL2}(E)$. This dependence is the most important feature of the nonlinear system as it is the very origin of the phenomenon "slow domains". For a stationary state without net carrier generation and with zero current divergence, the rate equation (eq. 2.4) is

$$g \cdot N_t^-(E) = c_{EL2}(E) n_{free}(E)[N_t - N_t^-(E)] \tag{4.10}$$

where the generation rate g is known to be field independent [34]. We know from our measurement that $\frac{N_t^-}{N_t}(E) \leq 10^{-4} \ll 1$. Together with the assumption $c_{EL2}(E) = c_0 \cdot c^*(E)$ this yields

$$c^*(E) = \frac{g}{c_0} \cdot \frac{\frac{N_t^-}{N_t}(E)}{n_{free}(E)} \tag{4.11}$$

While $n_{free}(E)$ is known by the fit eq. 4.9, the relation $\frac{N_t^-}{N_t}(E)$ is not directly accessible by our data. However, by connecting $N_t^-(x)$ to $E(x)$ as done in

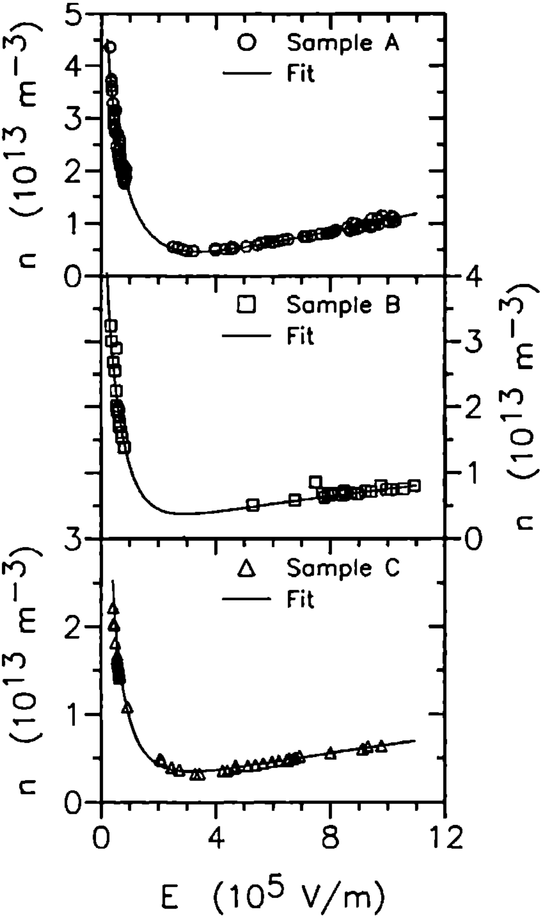

Figure 4.28:

Free carrier concentration n_{free} as a function of the electric field reconstructed for samples A, B and C

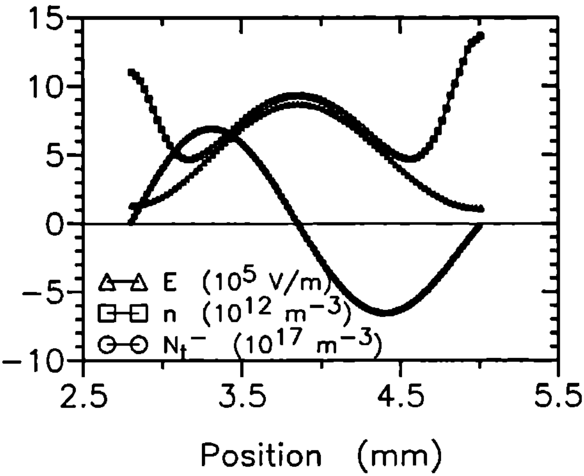

Figure 4.29:

$E(x)$ (derived of the measured $V(x)$), $N_t^-(x)$ (derived of $E(x)$) and $n_{free}(x)$ (reconstructed) for a typical recorded domain. $V_{exc} = 1000\,V$, $L = 6.45\,mm$. Note the different scales and in particular the small fraction of free carriers in respect to the charged traps.

Fig. 4.29 we can make two helpful statements: Firstly, N_t^- increases for low fields at least linearly with field. Secondly, N_t^- has a maximum at $E \approx 3 \cdot 10^5\,$V/m, but it is not clear whether it decreases or levels beyond this field.

Making the most simple approach $N_t^-(E) \sim E$ for $E \leq 3 \cdot 10^5\,$V/m and $N_t^-(E) = const.$ for $E > 3 \cdot 10^5\,$V/m, we arrive at a relation $c_{EL2}(E)$ which is pictured Fig. 4.30, together with the theoretical prediction of Barraud [48] which was used by Sacks and Milnes. Two main conclusions can be drawn from this figure: For the theoretical prediction as well as for our experimental reconstruction, the maximum variation of c_{EL2} is $c_{EL2,max}/c_0 \approx 10$. Additionally, both relations are in quite good agreement for the low-field range ($E \leq 2.5 \cdot 10^5\,$V/m) although our result reveals an onset of field-enhanced

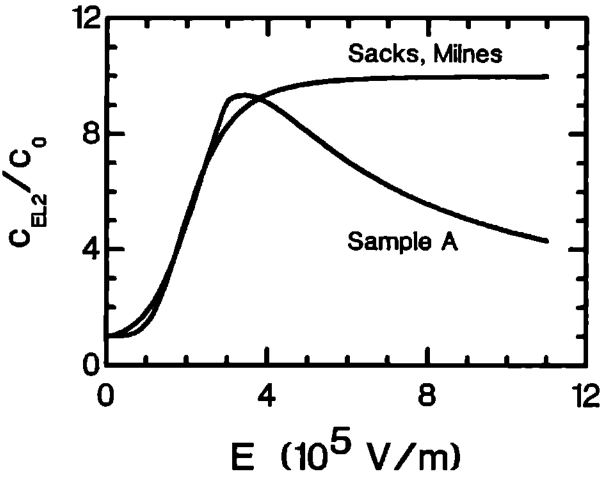

Figure 4.30:

Field dependence of the capture coefficient $c_{EL2}(E)$ (normalized to $c_{E=0}$) of the trap EL2 reconstructed for sample A and the one assumed by Sacks and Milnes (1970)

trapping at lower fields than predicted. So far, it is evident that the model of field-enhanced trapping is a good basis to explain slow domains.

The second conclusion is that the capture coefficient does not saturate at high fields but *decreases*, showing its maximum at $E \approx 3 \cdot 10^5$ V/m. It should be noted here, that the assumed field dependence of N_t^- is rather defensive and that a decrease of N_t^- towards higher fields would yield a even stronger decrease of c_{EL2} with field.

This is a fundamental difference to the models developed in the past and is the reason of all discrepancies observed between theory and our experimental data. The missing feature in the field-enhanced trapping model is that the trapping mechanism has to include a decreasing capture rate at high field. This decrease might be due to exited states of the traps, or that the carriers cannot loose their kinetic energy fast enough via phonon generation to be finally captured.

As for the drift velocity v_D of the domains, it was always found to increase with applied voltage but to differ in its absolute value from sample to sample. The velocities can however be correlated on a single curve by plotting them over the free carrier concentration at the center of the domain $n_{free}(E_{peak})$ (Fig. 4.31). v_D (in $10^{-3}\,\mathrm{m/s}$) can be fitted to $n_{free}(E_{peak})$ (in $10^{13}\,\mathrm{m}^{-3}$) by

$$v_D = a_1 \cdot n_{free}(E_{peak}) + a_2 \cdot \exp(a_3 \cdot n_{free}(E_{peak})) \tag{4.12}$$

where $a_1 = 11.2$, $a_2 = 0.0389$ and $a_3 = 6.36$. This is in direct contrast to the theoretical model of Sec. 2.2, which postulates that the velocity should be the velocity of free carriers reduced by the ratio of the free carriers at zero field and the involved traps n_0/N_t^- (eq. 2.13). It gives about the right order of magnitude for v_D and the dependency $v_D \sim n_0$ was confirmed by a number of other workers [9] [31] [11] [17]. Nevertheless, the relation $v_D \sim 1/N_t^-$ has been ruled out by our data, since Fig. 4.22b shows that N_t^- first increases and then decreases with domain size while the velocity steadily increases. By connecting eq. 4.12 to eq. 4.9 we can state that $v_D \sim n_{free}(E_{peak}) \sim E_{peak}$, as long as the domain grows in height. Beyond this size, the domains start to grow in width. To understand the physical connection to an exponential increase of v_D from there on, a closer theoretical analysis of the mechanisms determining the drift of a domain has to be performed.

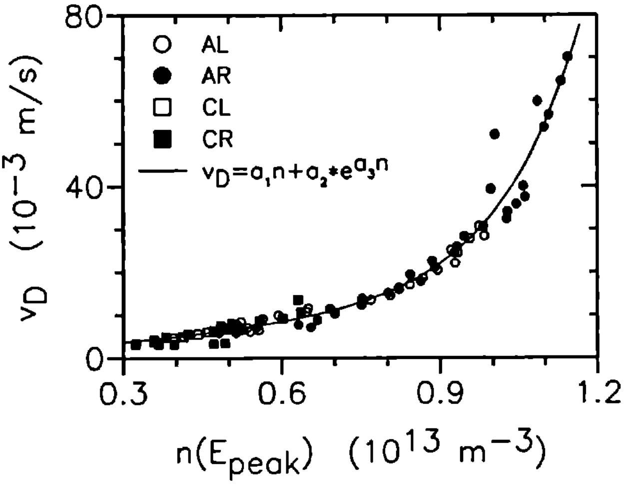

Figure 4.31 :

Drift velocity of the domains as a function of the free carrier concentration at the domain peak field. The parameters of the according fit are $a_1 = 11.2$, $a_2 = 0.0389$ *and* $a_3 = 6.36$.

5

Conclusion

In this work we presented new results of an experimental investigation of slow high-field domains in semi-insulating GaAs. These domains are an example of formation of spatial structure in a nonlinear system, where the electronic transport can no longer be described by homogeneous equilibrium mechanisms.

Although the subject is now thirty years old, no substantial progress towards a deeper understanding has been made during the last fifteen years. It is clear that for a system showing spatial structure, the experiments also have to provide data with a sufficient spatial resolution. As no such measurement technique has been available up to now, the theoretical models based on field-enhanced trapping have never been tested in detail.

To this means we developed a contactless, optical voltmeter which measures the potential distribution of a surface. We extended the known single-spot electrooptic voltage probing towards two dimensions, where a high performance CCD camera serves as the detector, and applied the technique to a new system. The resulting setup is capable of measuring voltage distributions $V(x,y,t)$ of high absolute accuracy with a temporal resolution of microseconds and a lateral one of micrometers. At the same time, the sensing light is prevented to interfere with the nonlinear behaviour of the sample. By this apparatus, we could for the first time measure the detailed features of slow domains in a very straightforward manner. We thereby could directly compare our results with the existing models.

In a first part of the experimental results, attention was given to the general phenomenology of domain formation. By connecting the current signal to the corresponding video frames, we could define four regimes of operation for a sample depending on the applied voltage. In the first regime, the whole sample is stable and the current shows no oscillations. The onset of the second regime is characterized by a critical voltage V_{c1} upon which small and noisy oscillations occur on the current. They are connected to weak domains which develop locally at the cathode and collapse within a range of $\approx 5\,\mathrm{mm}$. The third regime is marked by a second critical voltage V_{c2} and by the stable propagation of huge domains from the cathode to the anode. Finally, the sample shows electric breakdown in the fourth regime which was not further investigated. The clear definition of *two* critical voltages already demonstrates the capacity of our setup.

An excursion into the topology of domains revealed that the dynamics of stable domain propagation is highly influenced by the geometrical shape of the contacts. Here we found that the domains formed at a circular cathode spread as concentric rings through the sample without any preferential direction. Moreover, the current and field distributions of this geometry imply that the domains have a maximum radius for the distance to the cathode, eventually causing the domain to collapse before reaching the anode. This opens the field to a number of interesting experiments still to perform.

The quantitative part of our results is divided into two sections of which the first one focuses on the critical fields for onset of oscillations and on the temporal evolution of a domain cycle.

Generally, it was found that the simplified approach of applied critical voltage divided by the sample length which has been used up to now, heavily underestimates the real fields at the cathode. In particular, it was shown that V_{c1}, V_{c2} are in fact connected to two different critical fields which correspond to the two nonlinear subsystems: bulk GaAs and contact region. Exceeding the critical field ($E_{c1} \approx 0.5\,..\,1.25 \cdot 10^5\,\mathrm{V/m}$) of the contact region, weak domains can form and propagate. They cannot penetrate into the bulk sample, as the field of the latter is substantially higher, and are therefore restricted to the contact region of an extension of $\approx 0.5\,\mathrm{mm}$. While those domains produce only small sinoidal oscillations of the total current, the huge bulk domains which set in above the critical field of the bulk ($E_{c2} \approx 3.1\,..\,8.8 \cdot 10^5\,\mathrm{V/m}$) are extended over the whole width of the sample and result in distinct, pulse-shaped oscillations of the current.

The value ranges of the critical field suggest a carrier-injection nonlinearity for the contact domains. The corresponding range for bulk domains rather points to the Gunn-effect. Although a variety of contacts was investigated, no link between contact preparation and critical fields could be found.

Further on, we demonstrated the interaction between the subsystems during a complete stable domain cycle. It was shown that the peak of the current oscillations does not represent the maximum current density at the critical field for the bulk, as usually assumed. Instead, it is the response of the anode region to the high field imposed by the arriving and decaying domain. The often cited intermediate state of homogeneous field throughout the sample does not exist, because decay and growth of the domains at anode and cathode happen parallel in time. On the other hand, low current marks the domain being on transit through the sample. These results represent the first direct reconstruction of the detailed connection between the total current through the sample and the cycle of a domain reported so far.

The period of the current oscillation was shown to be composed of the transit time of the domain through the bulk and the decay time of the domain at the anode. The boundary condition of a constant integral of the electric field over the whole sample (constant voltage bias) could be shown to lead to an indirect interaction between the domains for suitable times where information about a domain is subsequently transferred to the following one. It will be most interesting to prove upon future experiments that this is the basic nonlinar mechanism for the routes to chaos observed in the current signal by other workers.

In the second section we concentrated on the investigation of stable domains propagating through bulk GaAs. We first established that the theoretical concept of the excess domain voltage is an integral measure of the domain size and is independent of both the particular shape of a domain and the geometry of a sample. The following, detailed analysis of the growth of a domain on this parameter showed that the model for domain formation based on field-enhanced trapping is incompatible with the data. The model predicts that for a sample showing a domain, its low-field part should be operated on a stable branch of the $j(E)$-characteristic whereas the domain is defined by an unstable high-field branch of $j(E)$ in analogy to Gunn domains. Contrary to this, our experimental results prove that both regions of the sample are operated on stable branches and that therefore the $j(E)$ of this material has to have a qualitatively different shape than the one proposed by theory. In detail, the amplitude of the domain grows linearly with the excess voltage until it saturates at $E \approx 10 \cdot 10^5\,\mathrm{V/m}$ but the domains do not become flat-topped further on as it is proposed by theory. The now increasing width is connected to the increasing distance between the peaks of the charge dipole which in turn becomes both wider and lower. This space charge of the domain was shown to consist almost entirely of ionized traps representing at most 0.01 % of the total trap concentration.

The knowledge of the basic shape of the $j(E)$-characteristic allowed us to connect the the total current through the sample to a corresponding set of two measured stable electric field values by $j(E_{low}) = j(E_{high})$. This enables us for the first time to constructed the two stable branches of $j(E)$ experimentally. The resulting characteristic is quite instructive and provides an explanation for the observed high-field limit of stable domains. Such a limit exists because the field far from the domain increases with the excess voltage until it eventually equals the critical field E_{c2} of the bulk. Exceeding this point, even the low-field parts of the sample become unstable which sharply changes the overall electric behaviour.

From $j(E)$ we could extract the nonlinear parameters which are substantial for the differences between slow domains and pure Gunn domains, namely the free carrier concentration $n_{free}(E)$ and the capture coefficient $c_{EL2}(E)$ of the involved deep trap. For fields below $E \approx 3 \cdot 10^5\,\mathrm{V/m}$, n_{free} is shown to decrease almost exponentially with field as it is to be expected for a trapping mechanism over a repulsive potential barrier. This decrease already sets in at fields lower than than our lowest measurement point ($E \approx 0.2 \cdot 10^5\,\mathrm{V/m}$). At $E \approx 3 \cdot 10^5\,\mathrm{V/m}$ the carrier concentration is at its minimum and increases about linearly with field further on.

The capture coefficient could be accessed only qualitatively by connecting $n_{free}(E)$ to the principal relation between ionized trap density and electric field. The latter could be roughly fixed to increase at least linearly with field for $E \leq 3 \cdot 10^5\,\mathrm{V/m}$ and to stay at most constant for higher fields. The characteristic $c_{EL2}(E)$ shows almost the same low-field behaviour as the theoretical characteristic used by previous workers which confirms the concept of field-enhanced trapping. Although the maximum field enhancements of the two are nearly identical ($c_{max}/c_0 \approx 10$), it is the high-field part which makes all the difference: Our characteristic clearly shows that the capture coefficient *decreases* above $E \approx 3 \cdot 10^5\,\mathrm{V/m}$ while up to now a simple saturation has been assumed. This explains the discrepancies between the existing models and our data very clearly.

Finally, it was found that the drift velocity of domains is correlated to the free carrier concentration at the centre of the domain. To explain this behaviour, a clear understanding of the drift mechanism has to be found. The empirical model with drift velocity inversely proportional to the density of ionized traps can be ruled out.

To sum up, we showed that a non-invasive optical voltage probing technique with high temporal and spatial resolution is by far superior to any other method employed up to now to investigate electronic systems with spontaneous structure formation. It allowed us for the first time to test the existing theories directly on the basis of experimental data not accessible in the past. Our data shows that the basic idea of field-enhanced trapping is a well chosen starting point. Nevertheless, we prove that the assumption of a constant capture coefficient at high fields made in the corresponding models is wrong so that important general predictions turn out not to be fulfilled. At this point of research it is important that the model is re-examined in order to adjust the nonlinear parameters to the experimental data.

6

Samenvatting

Niet-lineair Elektronisch Transport en Vorming van Strukturen in Halfgeleiders

In dit werk laten we nieuwe resultaten van experimenteel onderzoek aan trage hoog-veld domeinen in semi-isolerend GaAs zien. Deze domeinen zijn een voorbeeld van de vorming van een ruimtelijke struktuur in een niet-lineair systeem, waarvan het elektronische transport niet langer door homogene evenwichtsprocessen beschreven kan worden.

Alhoewel het onderwerp reeds een dertigtal jaren oud is, is het begrip ervan de laatste vijftien jaren niet beduidend toegenomen. Het mag duidelijk zijn dat experimenten aan een systeem met een ruimtelijke struktuur voldoende ruimtelijke oplossing moeten hebben. Aangezien zulke experimenten tot op heden nog niet voor handen waren, zijn de theoretische modellen gebaseerd op veld-versterkte invangst, nog nooit in detail getest.

Hiertoe hebben we een kontaktloze optische voltmeter ontwikkeld, welke de potentiaalverdeling over een oppervlak meet. We hebben de bekende elektro-optische volt meting op een punt, naar twee dimensies uitgebreid, waarvoor een zeer gevoelige CCD kamera dient als detektor, en we hebben de techniek op een nieuw systeem toegepast. De resulterende opstelling is in staat om spanningsverdelingen $V(x, y, t)$ met grote precisie te meten, met een tijdsoplossing van mikrosekonden en een ruimtelijke oplossing van mikrometers. Bovendien wordt het niet-lineaire gedrag van het preparaat niet door het metende licht beinvloed Met dit apparaat zijn we voor het eerst in staat om de details van trage domeinen op een direkte wijze te meten Onze resultaten kunnen zodoende direkt met de bestaande modellen vergeleken worden

In het eerste deel van het experimentele hoofdstuk is aandacht besteed aan de algemene fenomenologie van de vorming van domeinen Door de stroomsterkte met de overeenkomende videobeelden te verbinden, konden we vier, van de aangelegde spanning afhankelijke, regimes in het sample vastleggen In de eerste toestand is de gehele preparaat stabiel en de stroomsterkte vertoont geen oscillaties Karakteristiek voor het begin van het tweede regime is een kritieke spanning V_{c1} waarbij de stroom kleine en onregelmatige oscillaties vertoont Deze hangen samen met zwakke domeinen die zich plaatselijk aan de kathode ontwikkelen en na ongeveer 5 mm inzakken Het derde regime wordt gekenmerkt door een tweede kritieke spanning V_{c2} en door de stabiele voortplanting van grote domeinen van de kathode naar de anode Uiteindelijk vertoont het preparaat doorslag in het vierde bereik Dit is niet verder onderzocht Het duidelijke onderscheid van de twee kritieke spanningen demonstreert reeds de mogelijkheden van onze opstelling

Een diepergaande beschouwing van de topologie van de domeinen laat zien dat de dynamiek van stabiele domein voortplanting sterk wordt beinvloed door de geometrie van de kontakten We vonden hierbij dat domeinen die aan een cirkelvormige kathode gevormd worden, zich verspreiden als middelpuntsymmetrische ringen over het preparaat zonder enige voorkeursrichting Bovendien, vanwege de stroom en veldverdelingen bij deze geometrie, hebben de domeinen een maximale straal als afstand tot de kathode, wat inzakken van het domein kan veroorzaken voordat het de anode bereikt Dit laat een aantal mogelijkheden voor interessante experimenten open

De kwantitatieve resultaten zijn verdeeld in twee paragrafen waarvan de eerste gaat over de velden die kritiek zijn voor het ontstaan van de oscillaties en de tweede over de tijdsontwikkeling van een domein cyclus

Over het algemeen hebben we gevonden dat de aangebrachte kritieke spanning per preparaatlengte, wat tot nog toe een gebruikelijke maatstaf was, de werkelijke velden aan de kathode sterk onderschat Feitelijk hebben we laten zien dat V_{c1} en V_{c2} bij twee verschillende kritieke velden horen, die korresponderen met de twee niet lineaire subsystemen bulk GaAs en het kontaktgebied Bij overschrijding van het kritieke veld ($E_{c1} \approx 0\ 5\ \ 1\ 25\ \ 10^5$ V/m) in het kontaktgebied, kunnen zich zwakke domeinen vormen en voortplanten. Deze kunnen niet in het bulk materiaal doordringen, doordat het kritieke veld in de bulk beduidend hoger is, en ze zijn daardoor beperkt tot een zone van 5 mm vanaf het kontakt. Terwijl deze domeinen alleen kleine sinusoïdale oscillaties van de totale stroomsterkte produceren, zijn de grote bulk domeinen, welke opkomen vanaf het kritieke veld van de bulk ($E_{c2} \approx 3.1 .. 8.8 \cdot 10^5$ V/m), uitgebreid over de gehele breedte van het preparaat en ze resulteren in gescheiden, pulsvormige oscillaties van de stroomsterkte.

Het bereik van de diverse waarden van het kritieke veld suggereert een ladingsdrager-injektie niet-lineariteit over de kontaktdomeinen. Het bereik voor de bulkdomeinen echter, wijst naar het Gunn-effekt. Alhoewel een variatie van kontakten onderzocht is, werd er geen verband tussen kontaktpreparatie en kritieke velden gevonden.

Verder demonstreerden we de interaktie tussen de twee subsystemen gedurende een komplete stabiele domein cyclus. Er is aangetoond dat de piek van de stroomoscillaties niet de maximale stroomdichtheid bij de kritieke veldsterkte voor de bulk representeert, zoals gewoonlijk aangenomen werd. Het is echter de reaktie in het anodegebied door het sterke veld, dat door het aankomende en vervallende domein veroorzaakt wordt. De vaak geciteerde tussenliggende toestand van homogeen veld in het sample bestaat niet, want verval en groei van de domeinen aan anode en kathode gebeuren simultaan. Aan de andere kant is een lage stroom een indikatie dat het domein door het sample loopt. Deze resultaten representeren de eerste direkte rekonstruktie van het gedetailleerde verband tussen de totale stroom door het sample en de cyclus van een domein tot nu toe.

De periode van de stroomoscillaties bleek te bestaan uit de doorlooptijd van het domein door de bulk en de vervaltijd van het domein aan de anode. Er kan aangetoond worden dat de randvoorwaarde van een konstante integraal van het elektrische veld over het gehele sample (konstante bias spanning) leidt tot een indirekte wisselwerking tussen de domeinen op bepaalde tijden waarop informatie over een domein doorgegeven wordt aan het volgende. Het zou interessant zijn om in toekomstige experimenten te bewijzen dat dit het wezenlijke niet-lineaire mechanisme is voor de paden tot chaos zoals ze in de stroomsignalen door andere onderzoekers zijn waargenomen.

In het laatste deel van het experimentele werk richtten we onze aandacht op het onderzoek van de stabiele domeinen die zich door bulk GaAs voortplanten.

Het theoretische ontwerp van de excess domein spanning bevestigden we eerst als een volledige maat voor de domeingrootte en het is onafhankelijk van zowel de specifieke vorm van een domein als van de geometrie van het preparaat. De daaropvolgende gedetailleerde analyse van de groei van een domein met deze parameter, liet zien dat het model voor domeinvorming gebaseerd op veldversterkte invangst niet met de data overeenkomt. Voor een preparaat met een domein voorspelt het model dat het lage-veld gebiedje bij een stabiel deel van de $j(E)$-karakteristiek hoort, terwijl het domein veroorzaakt wordt door een instabiele hoog-veld branch van $j(E)$ in analogie met Gunn domeinen. In tegenstelling hiermee bewijzen onze experimentele resultaten dat beide gebiedjes van het preparaat op stabiele branches werken en dat daarom $j(E)$ van dit materiaal een kwalitatief andere vorm heeft dan door de theorie voorgesteld wordt. Meer precies, de amplitude van het domein groeit lineair met excess spanning totdat het verzadigd bij $E \approx 10 \cdot 10^5$ V/m, maar de domeinen worden vervolgens niet afgevlakt zoals door theorie voorgesteld wordt. De nu toenemende breedte hangt samen met de toenemende afstand tussen de pieken van de dipoollading, welke op zijn beurt zowel breder als geringer wordt. Naar bleek bestaat deze ruimtelading van het domein bijna volledig uit geioniseerde vangstcentra die hooguit 0,01 % van de totale dichtheid van vangstcentra uitmaken.

De kennis van de globale vorm van de $j(E)$-karakteristiek maakte het ons mogelijk om een verband te leggen tussen de totale stroomsterkte door het preparaat en een bijbehorende set van twee gemeten stabiele elektronische veldwaarden via $j(E_{laag}) = j(E_{hoog})$. Dit staat ons voor het eerst toe om de twee stabiele branches van $j(E)$ experimenteel te bepalen. De resulterende karakteristiek is zeer instruktief en geeft een verklaring voor de waargenomen hoog-veld limiet voor stabiele domeinen. Een dergelijke limiet bestaat, want het veld ver van het domain neemt toe met de excess spanning totdat het eventueel gelijk wordt aan de kritieke veld waarde E_{c2} in de bulk. Bij overschrijding van dit punt worden zelfs de laag-veld gebiedjes van het materiaal instabiel, hetgeen het gezamenlijke elektrische gedrag sterk zou veranderen.

Van $j(E)$ zouden we de niet-lineaire parameters, welke belangrijk zijn voor de verschillen tussen langzame domeinen en pure Gunn domeinen, af kunnen leiden, namelijk de vrije ladingsdrager dichtheid $n_{vrij}(E)$ en de vangst koefficient $c_{EL2}(E)$ van het betrokken diepliggende vangstcentrum. Voor velden lager dan $E \approx 3 \cdot 10^5$ V/m, neemt n_{vrij} bijna exponentieel met het veld af, zoals voor een invangst mechanisme door een afstotende potentiaal barriere te verwachten is. Deze afname begint al bij velden lager dan ons laagste meetpunt ($E \approx 0.2 \cdot 10^5$ V/m). Bij $E \approx 3 \cdot 10^5$ V/m bereikt de ladingsdrager dichtheid een minimum en neemt vervolgens min of meer lineair toe met de veldsterkte.

De koefficient voor invangst kan alleen kwalitatief verkregen worden door een verband te leggen van $n_{vrij}(E)$ met de hoofdzakelijke relatie tussen de dichtheid van ionen vangst centra en elektrisch veld. De laatste kan min of meer vastgelegd worden als een lineaire toename met de veldsterkte voor $E \leq 3 \cdot 10^5$ V/m en een hooguit konstante waarde voor hogere velden. De karakteristiek $c_{EL2}(E)$ laat bijna hetzelfde gedrag zien als de theoretische kurve welke voorheen door onderzoekers gebruikt werd, hetgeen het konsept van veldversterkte invangst bevestigd. Hoewel de maximale vergrotingen van het veld van de twee bijna identiek zijn ($c_{max}/c_0 \approx 10$), is het het hoog-veld aandeel dat het verschil uitmaakt: onze karakteristiek laat duidelijk zien dat de koefficient voor invangst *afneemt* boven $E \approx 3 \cdot 10^5$ V/m terwijl er tot nog toe een eenvoudige verzadiging aangenomen werd. Dit verklaart de verschillen tussen de bestaande metingen en onze data.

Tenslotte werd er gevonden dat de driftsnelheid van domeinen samenhangt met de vrije ladingsdrager dichtheid in het centrum van het domein. Om dit gedrag te verklaren, zou een helder begrip van het drift mechanisme gevonden moeten worden. Het empirische model met een driftsnelheid omgekeerd evenredig met de dichtheid van vangstcentra kan uitgesloten worden.

Alles bij elkaar opgeteld hebben we laten zien dat een niet-invasieve optische spanningsmeettechniek met hoge tijdelijke en ruimtelijke oplossing veruit superieur is aan enige andere tot op heden toegepaste methode om elektronische systemen met spontane strukturen te onderzoeken. Het stond ons voor het eerst toe om de bestaande theorieën direkt op basis van voorheen niet toegankelijke ideeën experimentele data te testen. Onze data laten zien dat het basisidee van veldversterkte invangst een goed gekozen uitgangspunt is. Niettemin hebben we bewezen dat de aanname van een konstante koefficient van invangst in hoge velden die in bepaalde modellen aangenomen wordt, onjuist is, zodat aan belangrijke algemene voorspellingen niet voldaan wordt. Op dit punt aangekomen is het van belang dat het model opnieuw beoordeeld wordt om de niet-lineaire parameters aan de experimentele gegevens aan te passen.

Appendix A

Electrooptics

A.1 Index Ellipsoid

Electrooptic and piezooptic effect reveal the influence of an externally imposed electric field or of an acoustic strain on the optical properties of a crystal. These effects are based on the fact that electric polarization **P** and electric field **E** in a crystal may not be collinear. In general, electric displacement **D** and **E** are coupled by the dielectric tensor ϵ_{kl} :

$$D_k = \epsilon_{kl} E_l \tag{A.1}$$

where $(k, l = 1{,}2{,}3)$ refer to the crystal axes[1]. By symmetry arguments of the Poynting theorem one can show that ϵ_{kl} is symmetric and has only six independent elements [49].

Taking the constant energy surfaces ω_E in a medium

$$\omega_E = \frac{1}{2\epsilon_0} \mathbf{E} \cdot \mathbf{D} \ , \tag{A.2}$$

application of eq. A.1 yields

$$2\epsilon_0 \omega_E = \frac{D_l D_k}{\epsilon_{kl}} \tag{A.3}$$

In order to eliminate the off-diagonal elements, one can perform a principal axes transformation and eq. A.3 becomes

$$2\epsilon_0 \omega_E = \sum_{k=1}^{3} \frac{D_k^2}{\epsilon_{kk}} \tag{A.4}$$

---

[1] Throughout this chapter, we will follow Einstein's summation convention

Normalizing eq. A.4 by $x_k := D_k(2\epsilon_0\omega_E)^{-\frac{1}{2}}$ and using the definition of the isotropic index of refraction $n^2 = \epsilon$ finally yields

$$1 = \sum_{k=1}^{3} \frac{x_k^2}{n_{kk}^2} \tag{A.5}$$

which describes an ellipsoid in **D**-space with the lengths of its major axes equal to $2n_{kk}$. Any axis of which its normal crossection through the origin of the ellipsoid is a circle is called an optical axis and light traveling along it will not undergo any change.

If a randomly polarized light beam travels along a non-optical axis, one can take apart its electric amplitude into components parallel to the direction of smallest and biggest index of refraction, which are given by the half-axes of the normal ellipse. As this corresponds to waves of different phase velocities, the resulting wave which leaves the crystal will show a phase shift in respect to the incident wave. This so-called birefringence is proportional to the length of the light path through the crystal. Many crystals (for example calcite) show natural or intrinsic birefringence. Its is widely used in constant phase shift devices ($\lambda/4$ and $\lambda/2$ retarders etc.) where the phase shift is chosen by an appropriate thickness of the crystal. In polarizers, the incoming beam is split due to its incident angle into two diverging beams of mutually orthogonal polarization, one of them being blocked out of the aperture of the following optical system.

A.2 Linear Electrooptic Effect

In general, the index ellipsoid of a crystal may be changed if an external electric field is applied. For convenience, one introduces the notation $\beta_{kl} = (1/n^2)_{kl}$. This can be reduced further due to the interchange symmetries of $\epsilon_{\mathbf{kl}}$ and $(\mathbf{1/n^2})_{\mathbf{kl}}$ by use of the contracted matrix notation $(1,1) \rightarrow 1$; $(2,2) \rightarrow 2$; $(3,3) \rightarrow 3$; $(2,3) \rightarrow 4$; $(1,3) \rightarrow 5$; $(1,2) \rightarrow 6$. In order to remember the rank of the involved tensors, we will use latin letters for indices running from 1..3 and greek letters for those running from 1..6. Therefore, $\mathbf{a_{lm}}$ (or, in the symmetric case, $\mathbf{a}_\lambda$), $\mathbf{a}_{\lambda\mathbf{m}}$, $\mathbf{a}_{\lambda\mu}$ indicate second-, third- and fourth-rank tensors, respectively.

The linear electrooptic (Pockels-) effect describes the change of the $\Delta\beta_k$ by

$$\Delta\beta_\lambda = r_{\lambda m} E_m \tag{A.6}$$

with $\mathbf{r}_{\lambda \mathbf{m}}$ as the third-rank electrooptic tensor (the first subscript in contracted notation) and $\mathbf{E}$ a quasi-static electric field. Simple symmetry consideration reveals that only crystals without inversion symmetry (piezoelectric crystals) may show non-vanishing elements of $\mathbf{r}_{\lambda \mathbf{m}}$. Application of eq. A.5 and eq. A.6 yields in the most general case

$$1 = \sum_{k=1}^{3} (\beta_k + \Delta\beta_k) x_k^2 + 2\Delta\beta_4 x_2 x_3 + 2\Delta\beta_5 x_1 x_3 + 2\Delta\beta_6 x_1 x_2 \tag{A.7}$$

which means that both the orientation of the index ellipsoid and the lengths of its axes change under influence of an electric field. One has to perform another principal axis transformation to obtain the new principal axes, which may turn out to be quite complicated for a random crystal symmetry group and random orientation $\mathbf{E}$. However, as we will here only deal with crystals of high symmetry and isotropic index of refraction in the undisturbed case, the changes of β_λ are easy to compute.

For GaAs which belongs to the $\bar{4}3m$ symmetry group, eq. A.5 reduces to the sphere

$$1 = \beta_0 \sum_{k=1}^{3} x_k^2 \tag{A.8}$$

where x_k correspond to the principal crystal axes. For crystals of this group, $\mathbf{r}_{\lambda \mathbf{m}}$ has only three non-vanishing elements so that eq. A.7 takes the form

$$\begin{pmatrix} \Delta\beta_1 \\ \Delta\beta_2 \\ \Delta\beta_3 \\ \Delta\beta_4 \\ \Delta\beta_5 \\ \Delta\beta_6 \end{pmatrix} = \begin{pmatrix} 0 & 0 & 0 \\ 0 & 0 & 0 \\ 0 & 0 & 0 \\ r_{41} & 0 & 0 \\ 0 & r_{41} & 0 \\ 0 & 0 & r_{41} \end{pmatrix} \cdot \begin{pmatrix} E_1 \\ E_2 \\ E_3 \end{pmatrix} \tag{A.9}$$

Applying the electric field for example in x_3-direction, eq. A.8 changes into

$$1 = \beta_0 \sum_{k=1}^{3} x_k^2 + 2 r_{41} E_3 x_1 x_2 \tag{A.10}$$

The principal axis transformation of eq. A.10 now simply consists of a rotation of eq. A.8 by $\pi/4$ around x_3 which gives

$$1 = (\beta_0 + \Delta\beta_6)x_1'^2 + (\beta_0 - \Delta\beta_6)x_2'^2 + \beta_0 x_3'^2 \tag{A.11}$$

To compute n_1', n_2', one uses the differential equation

$$\frac{d\beta_0}{dn_0} = -\frac{2}{n_0^3} \ for \ (\Delta\beta_0 \ll \beta_0) \tag{A.12}$$

and obtains

$$n_1' = n_0 - \frac{n_0^3}{2}\Delta\beta_6 \ ; \ n_2' = n_0 + \frac{n_0^3}{2}\Delta\beta_6 \tag{A.13}$$

One has now all information to evaluate the propagation of light through the crystal. If the light wave propagates along x_3 with a linear polarization parallel to x_1 (and therefore in the new axis system in the x_1'-x_2' plane with an angle of $\pi/4$ to x_1), the optical field can be split into two components parallel to x_1' and x_2', respectively. Due to eq. A.13, both waves travel with different phase velocities and will leave the crystal of a thickness d with the phase shift Γ (also called retardation)

$$\begin{aligned} \Gamma &= (\omega t - \frac{\omega}{c}n_1'd) - (\omega t - \frac{\omega}{c}n_2'd) \\ &= \frac{2\pi}{\lambda}n_0^3 r_{41} E_3 d \end{aligned} \tag{A.14}$$

where λ is the vacuum wave length of the incident light. For $\Gamma = \pi/2$, light is circulary polarized when leaving the crystal (the two orthogonal waves are relatively displaced by $\lambda/4$), whereas for $\Gamma = \pi$ the polarization is again linear but now along x_2.

To consider other orientations, [39] gives the general expression for cubic crystals

$$\begin{aligned} \Delta n^+ &= -\frac{1}{2}n_0^3 \mathbf{e} \cdot \mathbf{\Delta\beta_k} \cdot \mathbf{e} \\ \Delta n^- &= -\frac{1}{2}n_0^3 (\mathbf{e} \times \mathbf{s}) \cdot \mathbf{\Delta\beta_k} \cdot (\mathbf{e} \times \mathbf{s}) \end{aligned} \tag{A.15}$$

and

$$\Gamma = \frac{2\pi d}{\lambda}(\Delta n^+ - \Delta n^-) \tag{A.16}$$

with $\Delta n^\pm$ the effective changes of the indices of refraction for light traveling parallel to the unit vector s and polarization along the unit vector e, both taken in the crystal axis system.

Appendix B

Piezooptics and its Coupling to Electrooptics

B.1 Linear Piezooptic Effect

Similar to the way an electric field acts via the electrooptic effect onto a crystal, one can introduce birefringence by application of mechanical stress or strain to the crystal.

To describe this so-called piezooptic effect, the stress tensor $\mathbf{T}_{\mathrm{kl}}$ is coupled to the β_{ij} by the fourth-rank piezooptic tensor $\mathbf{q}_{(\mathrm{ij})(\mathrm{kl})}$ which yields in contracted notation

$$\Delta\beta_\lambda = q_{\lambda\mu} T_\mu \tag{B.1}$$

Here, $\mathbf{T}_\mu$ is of the same symmetry as β_λ with $T_1..T_3$ representing normal stress components and $T_4..T_6$ shear stress components. (A description by the strain tensor $\mathbf{S}_\mu$ and the elastooptic tensor $\mathbf{p}_{\lambda\mu}$ is fully equivalent). The combination of eq. A.15, eq. A.16 and eq. B.1 allows to determine the phase retardation for any direction of the light path and the applied stress.

As for the dependence of $\mathbf{q}_{\lambda\mu}$ on the crystal symmetry, this case is more complicated than for the electrooptic effect because principally also crystals with inversion symmetry show piezooptic effect. As a result, this effect is widely used as a technique for stress analysis in mechanical engineering and quality control. But furthermore, even the most simplest crystal group $\bar{4}3m$

shows 12 nonvanishing elements of $\mathbf{q}_{\lambda\mu}$, three of them being independent:

$$\mathbf{q}_{\lambda\mu} = \begin{pmatrix} q_{11} & q_{12} & q_{12} & 0 & 0 & 0 \\ q_{12} & q_{11} & q_{12} & 0 & 0 & 0 \\ q_{12} & q_{12} & q_{11} & 0 & 0 & 0 \\ 0 & 0 & 0 & q_{44} & 0 & 0 \\ 0 & 0 & 0 & 0 & q_{44} & 0 \\ 0 & 0 & 0 & 0 & 0 & q_{44} \end{pmatrix} \tag{B.2}$$

B.2 Coupling of Electrooptic and Piezooptic Effect

Up to now, electrooptic and piezooptic effects have been treated as linearly independent, i.e.

$$\Delta\beta_\lambda = r_{\lambda m}^{(\mathbf{T})} E_m + q_{\lambda\mu}^{(\mathbf{E})} T_\mu \tag{B.3}$$

where the superscripts indicate the variables to be held constant for the independent treatment. There exists a third independent effect which is called the rotooptic effect. It consists in the antisymmetric combination of displacement gradients as they are given by the infinitisimal rotation tensor. However, for the cubic crystals we are interested in here all elements of the rotooptic tensor vanish and one can therefore omit this effect.

In general, if one does experiments on birefringence and specially if one uses birefringence as a diagnostic tool as we do, eq. B.3 is not fullfilled because the variables to be held constant cannot be controlled. If possible, one chooses a direction of light in respect to the crystal axes which shows no birefringence due to piezooptics if for example one works with electrooptics. Problems of equivocality arise if such a orientation cannot be found (or used). Another problem one has to face is the fact that, in electrooptic active crystals, electric fields couple with the piezoelectric effect to introduce mechanical stress, which in turn gives rise to an indirect piezooptic effect. This indirect piezooptic effect may be of the same order of magnitude as the electrooptic one, but still more complications may arise as both can have opposite signs. To decide most easily about the origin of an observed phase shift (or phase shift pattern for the two-dimensional case), one can rotate the polarization vector of the incident light beam in respect to the crystal and compare the symmetries of the different obtained phase shift patterns with computations of the index ellipsoid (eq. A.15) based on the different effects. However, one often has a contribution of both terms in eq. B.3 as well as from the indirect piezooptic effect so that a quantitative connection of the phase shift to electric fields or mechanical stresses may be impossible.

In order to understand the origin of the indirect piezooptic effect, one can take the definition of the tensor of piezoelectric stress coefficients $\mathbf{e}_{\mathbf{m}\lambda}$ which relates the stress output to an applied electric field as

$$T_\lambda = -e_{m\lambda} E_m \tag{B.4}$$

(an equivalent expression relates the strain output to the field). For the $\bar{4}3m$ group, $\mathbf{e}_{\mathbf{m}\lambda}$ is of the same symmetry like $\mathbf{r}_{\lambda\mathbf{m}}$ (although transposed) so that one is left with the three elements $e_{14} = e_{25} = e_{36}$. Eq. B.4 directly shows that in a $\bar{4}3m$ crystal the stress produced by an electric field is always shear stress.

Putting eq. B.4 into eq. B.3 yields

$$\Delta\beta_\lambda = r_{\lambda m} E_m - q_{\lambda\mu} e_{m\mu} E_m + q_{\lambda\mu} T_\mu \tag{B.5}$$

with the second term as the indirect piezooptic effect. To illustrate its influence, the example of section A.2 can be taken again with an electric field applied in x_3-direction. Omitting the direct piezooptic effect, eq. B.5 gives

$$\begin{aligned} \Delta\beta_\lambda &= 0 \ , \ \lambda = 1,2,3,4,5 \\ \Delta\beta_6 &= (r_{41} - q_{44} e_{14}) E_3 \end{aligned} \tag{B.6}$$

In the case of an infinite crystal, this means a correction in the order of 3.5 % for r_{41} in GaAs [39][50]. Here, passing a light beam in x_3-direction would still allow to deduce the potential values from the phase shift. In a transverse setup, i.e. the light beam parallel to the x_1-direction, one would not detect any retardation at all as this is an optical axis.

The situation changes drastically if one works with a finite sample which is limited for example in x_1-direction to the usual wafer thickness of 0.5 mm. Although the stress induced by the piezoelectric effect is a shear stress on the x_1– and x_2–planes, this stress has to be partly transformed into normal stress at the surface of the sample in order to balance displacements (Figure B.1).

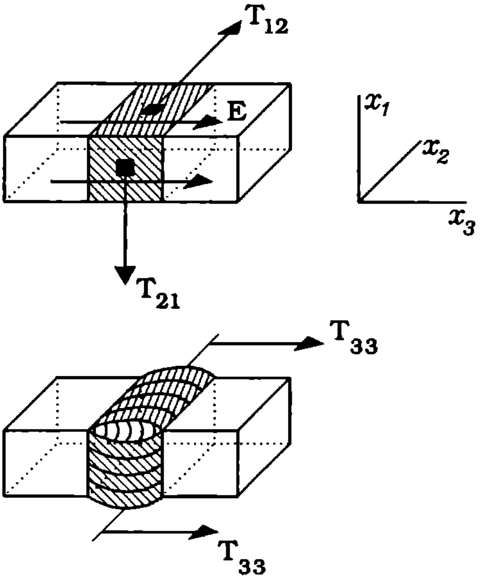

Figure B.1 :
Transformation of shear stresses T_{12} and T_{21} into normal stress T_{33} at the surface of a finite sample

The main component of this normal stress will be T_3 and eq. B.5 together with eq. B.2 yields

$$\begin{aligned}\Delta\beta_1 &= q_{11}T_3\\ \Delta\beta_2 &= q_{12}T_3\\ \Delta\beta_3 &= q_{11}T_3 = \Delta\beta_1\\ \Delta\beta_6 &= (r_{41} - q_{44}e_{14})E_3 \qquad \text{(B.7)}\end{aligned}$$

From this it is obvious that, namely as T_3 has no controlled value, it should be difficult to read E_3 from the phase shift of a longitudinal setup. For the transverse case, x_1 is no longer an optical axis in the vicinity of the two surfaces and one will observe a non neglectible retardation. In fact, for GaAs the amplitude of this phase shift due to surface deformations can be of the same order of magnitude as the one resulting from a longitudinal setup with an infinite crystal.

Bibliography

[1] T.B.Watkins and B.K.Ridley. *Proc.Phys.Soc.*, 78:293, 1961.

[2] J.B.Gunn. *Solid-State Comm.*, 1:38, 1963.

[3] B.W.Knight and G.A.Peterson. *Phys.Rev.*, 147:617, 1966.

[4] B.W.Knight and G.A.Peterson. *Phys.Rev.*, 155:393, 1967.

[5] A.Barraud. *C.R.Acad.Sci.Paris*, 256:3632, 1963.

[6] D.C.Northrop, P.R.Thornton, and K.E.Trezise. *Solid-State Electron.*, 7:17, 1964.

[7] H.K.Sacks and A.G.Milnes. *Int.J.Electronics*, 28:565, 1970.

[8] B.K.Ridley and P.H.Wisbey. *Brit.J.Appl.Phys.*, 18:761, 1967.

[9] G.N.Maracas et al. *Physica*, 134B:276, 1985.

[10] J.Lusakowski et al. *Acta Physica Polon.*, A73:183, 1988.

[11] W.Knap et al. *Solid-State Electron.*, 31:813, 1988.

[12] J.Požela. *Plasma and Current Instabilities in Semiconductors.* Pergamon Press, Oxford, 1981.

[13] E.Schoell. *Physica Scripta*, T29:152, 1989.

[14] M.P.Shaw, V.V.Mitin, E.Schoell, and H.L.Grubin. *The Physics of Instabilities in Solid State Electron Devices.* Plenum Press, New York, 1992.

[15] G.N.Maracas et al. *Solid-State Electron.*, 32:1887, 1989.

[16] D.A.Johnson et al. *Appl.Phys.Lett.*, 51:1152, 1987.

[17] H.Rajbenbach, J.M.Verdiell, and J.P.Huignard. *Appl.Phys.Lett.*, 53:541, 1988.

[18] U.Rau et al. *Phys.Lett.*, A152:356, 1991.

[19] H.K.Sacks and A.G.Milnes. *Int.J.Electronics*, 30:49, 1971.

[20] P.F.Fontein, P.Hendriks, and J.H.Wolter. *Surf.Science*, 229:47, 1990.

[21] K. de Kort. Philips NatLab. Eindhoven. private communication.

[22] S.Larigaldie. *J.Appl.Phys.*, 61:90 and 102, 1987.

[23] P.Uhlig, J.C.Maan, and P.Wyder. *Phys.Rev.Lett.*, 63:1968, 1989.

[24] E.Schoell. *Physica*, 134B:271, 1985.

[25] J.Peinke. *Nichtlineariteaten und Chaos beim Elektronentransport in Halbleitern.* PhD thesis, Universitaet Tuebingen, 1988.

[26] E.G.Gwinn and R.M.Westervelt. *Phys.Rev.Lett.*, 57:1060, 1986.

[27] D.E.McCumber and A.G.Chynoweth. *IEEE Trans.Electron.Devices*, ED-13:4, 1966.

[28] M.F.Leach and B.K.Ridley. C11:2265, 1978.

[29] M.Eizenberg and H.J.Hovel. *J.Appl.Phys.*, 69:2256, 1991.

[30] J.C.Manifacier and H.K.Henisch. *J.Appl.Phys.*, 52:5195, 1981.

[31] D.A.Johnson, R.A.Puechner, and G.N.Maracas. *J.Appl.Phys.*, 67:300, 1990.

[32] N.Derhacobian and N.M.Haegel. *Phys.Rev.*, B44:12754, 1991.

[33] B.K.Ridley, J.J.Crisp, and F.Shishiyanu. *J.Phys.*, C5:187, 1972.

[34] S.Makram-Ebeid and M.Lannoo. *Phys.Rev.B*, 25:6406, 1982.

[35] P.Hendriks et al. *Appl.Phys.Lett.*, 54:1763, 1989.

[36] Z.H.Zhu et al. *Appl.Phys.Lett.*, 49:432, 1986.

[37] Z.H.Zhu et al. *Appl.Phys.Lett.*, 50:1228, 1987.

[38] Y.H.Lo et al. *Appl.Phys.Lett.*, 50:1125, 1987.

[39] Landolt-Boernstein. *Piezo-Optic and Related Constants*, volume III/11.

[40] R.E.Aldrich, S.L.Hou, and M.L.Harvill. *J.Appl.Phys.*, 41:493, 1970.

[41] J.Lusakowski. *Materials Science and Engineering*, B6:1, 1990.

[42] J.Požela et al. *Appl.Phys.*, A48:181, 1989.

[43] B.K.Ridley and R.G.Pratt. *Phys.Lett.*, 4:300, 1963.

[44] M.J.Feigenbaum. *Physica*, 7D:16, 1983.

[45] K.Karpińska and J.Lusakowski. *Acta Physica Polon.*, A80:425, 1991.

[46] J.Požela, A.Tamaševičius, and J.Ulbikas. *Solid-State Electron.*, 31:805, 1988.

[47] J.G.Ruch and G.S.Kino. *Appl.Phys.Lett.*, 10:40, 1967.

[48] A.Barraud. Clearinghouse for Scientific and Technical Information, PhD Thesis. Va.22151, N69-18810-3/26.

[49] A.Yariv. *Quantum Electronics.* John Wilsey & Sons Inc., 2nd edition, 1975.

[50] A.Feldman and D.Horowitz. *J.Appl.Phys.*, 39:5597, 1968.

Curriculum Vitae

Bert Willing

06.06.1964	born in Neuburg a.d. Donau, FRG son of Peter Willing and Marianne, née Bieber
9/70 - 4/72	Grundschule Neuburg a.d. Donau, FRG
5/72 - 8/74	Grundschule Lutzerath, FRG
9/74 - 5/75	Gymnasium Cochem, FRG
6/75 - 6/83	Gymnasium Sobernheim, FRG
21.06.1983	Allgemeine Hochschulreife (Matura)
7/83 - 9/83	Practical training as a technician (metal tooling) D.W.Renzmann, Monzingen, FRG
10/83 - 3/84	Study of Physics, Universität Mainz, FRG
4/84 - 5/90	Study of Physics Technische Universität Braunschweig, FRG
06.10.1985	Vordiplom Physik (BSc Physics)
07.05.1990	Diplom Physik (MSc Physics)
since 01.06.1990	Scientific staff position at the Max-Planck-Institut für Festkörperforschung, Hochfeld-Magnetlabor Grenoble, France